This manuscript is a preprint and has been submitted for publication in *Earthquake Spectra*. Take into consideration that the manuscript has yet to be formally accepted for publication and may have slightly different content between the preprint and accepted version. The final version of this manuscript will be available via the publication DOI link. Please feel free to contact any of the authors for more information.

Quantifying relationships between fault parameters and rupture characteristics associated with thrust and reverse fault earthquakes.

Kristen Chiama[1,2], William Bednarz[2], Robb Moss[3], Andreas Plesch[2], John H. Shaw[2]

We investigate the influence of earthquake source characteristics and geological site parameters on fault scarp morphologies for thrust and reverse fault earthquakes using geomechanical models. We performed a total of 3,434 distinct element method (DEM) model experiments to evaluate the impact of the sediment depth, density, homogeneous and heterogeneous sediment strengths, fault dip, and the thickness of unruptured sediment above the fault tip on the resultant ground surface deformation during a thrust or reverse fault earthquake. We used a computer vision (CV) model to obtain measurements of ground surface deformation characteristics (scarp height, uplift, deformation zone width, and scarp dip) from a total of 346,834 DEM model stages taken every 0.05 m of slip. The DEM dataset exhibits a broad range of scarp behaviors, including monoclinal, pressure ridge, and simple scarps – each of which can be modified by hanging wall collapse. The parameters that had the most influence on surface rupture patterns are fault displacement (i.e., anticipated earthquake magnitude), fault dip, sediment depth, and sediment strength. The DEM results comprehensively describe the range of historic surface rupture observations in the Fault Displacement Hazards Initiative (FDHI) dataset with improved relationships obtained by incorporating additional information about the earthquake size, fault geometry, and surface deformation style. We suggest that this DEM dataset can be used to supplement field data and help forecast patterns of ground surface deformation in future earthquakes given specific anticipated source and site characteristics.

INTRODUCTION

The surface deformation observed in large magnitude thrust and reverse fault earthquakes has a substantial impact on the built environment, including energy and transmission infrastructure, transportation systems, and other critical lifelines (Fig. 1) (Youngs et al., 2003; Wesnousky, 2008; Petersen et al., 2011; Moss and Ross, 2011; Boncio et al., 2018; Baize et al., 2019; Chen and Petersen, 2019). Recent thrust and reverse fault events such as the 1988 M 6.9 Spitak, Armenia, 1999 M 7.6 Chi-Chi, Taiwan, 2008 M 7.9 Wenchuan, China, and 2013 M 7.2 Bohol, Philippines, earthquakes featured complex rupture characteristics such as coseismic folding, secondary faulting, backthrusts, and distributed fracturing (Philip et al., 1992; Kelson et al., 2001; Hubbard and Shaw, 2009; Xu et al., 2009; Boncio et al., 2018; Rimando et al., 2019). Identifying patterns of potential future ground surface ruptures to better design and prepare infrastructure is an active area of research, specifically within the Probabilistic Fault Displacement Hazard Assessments

[1] Corresponding Author: Kristen Chiama (kchiama@g.harvard.edu).
[2] Harvard University, Dept. of Earth and Planetary Sciences, 20 Oxford St, Harvard University, Cambridge MA 02138.
[3] California Polytechnic State University, Dept. of Civil and Environmental Engineering, 1 Grand Avenue, San Luis Obispo, CA 93407.

(PFDHA) community (Wells and Coppersmith, 1994; Youngs et al., 2003; Wesnousky, 2008; Petersen et al., 2011; Moss and Ross, 2011; Boncio et al., 2018; Sarmiento et al., 2021). Nevertheless, the dataset of measured ground surface ruptures is quite limited, with 25 thrust or reverse fault events recorded in the Fault Displacement Hazards Initiative (FDHI) dataset (Sarmiento et al., 2021). Given the limited availability of measured natural ruptures, it is difficult to develop meaningful statistical relationships between geological site characteristics (fault dip, sediment strength, sediment depth to bedrock, earthquake magnitude, etc.) and the resultant ground surface rupture characteristics (primary rupture deformation zone width, scarp height, scarp dip, etc.). Therefore, we lack the ability to effectively forecast many aspects of surface fault rupture morphology in ways that can inform design and placement of critical infrastructure.

Numerical models can closely reproduce natural behaviors of deformation including fault propagation through near-surface sediment, fracturing, folding, backthrusts, uplift, tensile fractures, and hanging wall collapse (Strayer and Hudleston, 1997; Finch et al., 2003, 2004; Imber et al., 2004; Strayer et al., 2004; Hardy and Finch, 2005, 2007; Benesh et al., 2007; Hughes and Shaw, 2014, 2015; Morgan, 2015; Garcia and Bray, 2018a, 2018b; Hughes, 2020; Hardy and Cardozo, 2021; Chiama et al., 2023; Benesh and Shaw, 2023). Specifically, models based on the distinct element method (DEM) allow for emergent faulting behaviors driven by displacement of boundary conditions in mechanically realistic sedimentary sections (Garcia and Bray, 2018a, 2018b; Hughes, 2020; Chiama et al., 2023; Benesh and Shaw, 2023). DEM models offer the ability to interrogate the resultant deformation for additional information such as the precise magnitude and distribution of strain, displacement as well as velocity of individual particles, and breakage of contact bonds between particles – information that cannot readily be obtained from analog models (Morgan, 1999, 2004; Garcia and Bray, 2018a; Chiama et al., 2023). This information provides direct insights into the mechanics of deformation that helps better understand processes of deformation across a range of scales.

We build on the analysis by Chiama et al. (2023) where they employed DEM to explore the characteristics of deformation that result from surface ruptures during large thrust and reverse fault earthquakes. They presented models that effectively reproduced the characteristics of three main classes of fault scarps (monoclinal, pressure ridge, and simple) that could be modified by surface collapse (slumping, tensile fracturing). The DEM models in Chiama et al. (2023) were calibrated by replicating analog sandbox fault models (Cole and Lade, 1984; Bransby et al., 2008) as well as 3D DEM models (Garcia and Bray, 2018a, 2018b), and highlighted key parameters (slip magnitude, fault dip, sediment strength) that led to specific styles of surface deformation. Herein, we extend their study to thousands of models resulting in 346,834 model measurements. We use these results to compare with and supplement field observations in order to provide a robust dataset of ground surface rupture measurements that can serve as a basis for statistical relationships between earthquake parameters, site properties (e.g., sediment composition), and ground rupture characteristics (e.g., scarp height, width, and slope). These data will aid in better forecasting the hazards associated with the potential surface rupture in future earthquakes.

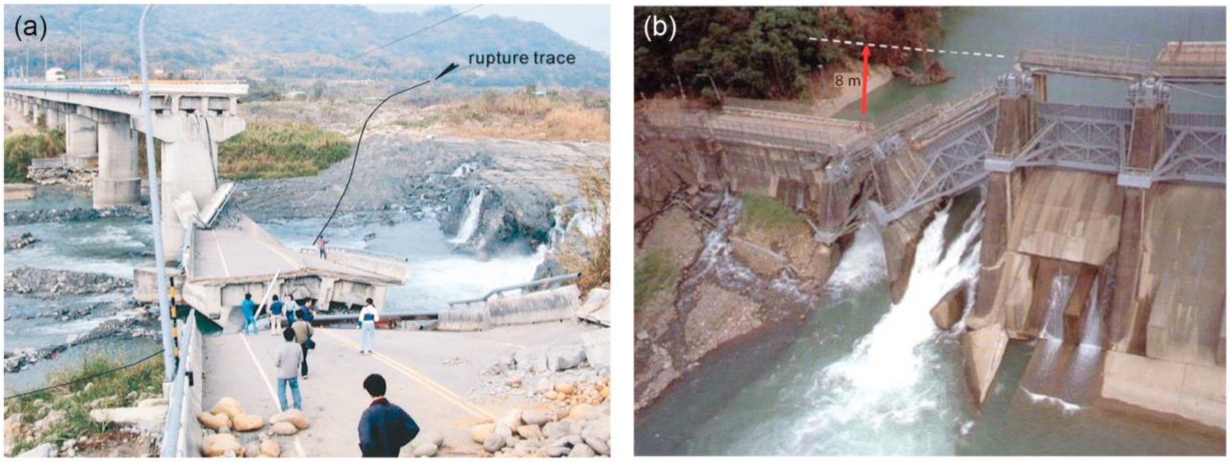

Fig. 1. Images of surface ruptures associated with coseismic thrust fault displacements during the 1999 M 7.6 Chi-Chi, Taiwan, earthquake. (a) Offset river along the Chelungpu fault led to a collapsed bridge (Chen et al., 2001); and (b) damaged Shih-Kang Dam due to ~8 m of uplift on the Chelungpu fault (Faccioli et al., 2008).

FAULT SCARP MORPHOLOGIES

Chiama et al. (2023) presented an initial suite of 45 DEM (within the family of discrete element method) model experiments to evaluate the impact of the fault dip (20º, 40º, 60º) and sediment strength (cohesion equal to tensile strength: 0.1 - 2.0 MPa) in dense, 5 m deep sediment. These experiments revealed 3 main types of fault scarp morphology: 1, monoclinal scarps, 2, pressure ridge scarps, 3, simple scarps (Fig. 2a,c,e; Chiama et al., 2023). Each scarp type has a version that is subsequently modified by hanging wall collapse (Fig. 2b,d,f in Chiama et al., 2023). Examples of these scarp morphologies have been well-documented in recent earthquakes such as the 1988 Armenian, 1999 Chi-Chi, Taiwan, 2008 Wenchuan, China, and 2016 Kaikoura, New Zealand earthquakes (Philip et al., 1992; Kelson et al., 2001; Hubbard and Shaw, 2009; Xu et al., 2009; Boncio et al., 2018; Litchfield et al., 2018).

Monoclinal scarps form inclined dip slopes that are limited by the angle of repose of the sediment (Fig. 2a). Monoclinal scarps form through distributed shear of the sediment above the fault tip which yields folding of the sedimentary layers via fault-propagation folding (Erslev, 1991; Allmendinger, 1998; Hardy and Finch, 2007; Hughes and Shaw, 2015). The dip of the surface slope within the scarp generally increases with fault slip until it reaches the angle of repose of the sediment. This process results in a smooth, single dip panel that characterizes monoclinal scarps (Chiama et al., 2023). These monoclinal scarps tend to form on a fault that dips more steeply than the friction angle of the sediment and in sediments that are sufficiently weak to promote distributed shear, as opposed to localized faulting. Monoclinal scarps are commonly observed in thrust and reverse fault ruptures around the world, including the 2008 M 7.9 Wenchuan, China and 2013 M 7.2 Bohol, Philippines earthquakes (Fu et al., 2011; Rimando et al., 2019). In comparison, when the sediment is stronger, the slip will become more localized to distinct shear bands above the fault tip which yields multiple localized dip panels within broader monoclinal scarps. Moreover, stronger sediments tend to deform at the surface by tensile fracturing and normal faulting, which generates distinct blocks of colluvium that rotate into the base of the scarp (Fig. 2b). The collapse of these monoclinal scarps produces distinct surface morphologies that have been observed in the

1988 M 6.9 Armenian earthquake (Institute of Geological Sciences, Republic of Armenia, 1988), and other events worldwide.

Pressure ridge scarps feature folding and uplift due to the presence of additional fault splays, typically including back thrusts (Fig. 2c). These scarps have a region of localized uplift above the fault traces due to the combination of slip on a forethrust and backthrust. In some cases, the backthrusts accommodate a significant component of the total fault slip as they are better oriented for failure when the primary fault dip is less than the friction angle of the sediment. The pressure ridge scarps that are modified by hanging wall collapse generate tensile fractures at the highest point of uplift and folding which creates distinct blocks of colluvium at the base of the scarp (Fig. 2d). The 1999 M7.6 Chi-Chi, Taiwan earthquake ruptured along the shallowly dipping Chelungpu fault and generated pressure ridge scarps with a smooth surface expression of broad uplift due to coseismic folding (Fig. 2c; Chen et al., 2001). In addition, this rupture produced pressure ridge collapse scarps with brittle fracturing and blocks of colluvium that collapsed into the base of the scarp in more cohesive sediment (Fig. 2d) (Lee et al., 2001).

Simple scarps represent cases in which the ground surface is directly offset by the fault plane (Fig. 2e). In these cases, the sediment is strong enough to resist gravitational collapse and maintains a fault scarp overhang with a scarp dip equivalent to that of the fault at depth. A simple scarp was observed in the 2008 M 7.9 Wenchuan earthquake along the Beichuan fault rupture. The fault plane dipping ~75º – 80º was preserved in this scarp with striations indicating the slip direction and the ground surface offset reflecting ~ 3 m of vertical displacement (Fig. 2e) (Li et al., 2010). At this site, the sediment had sufficient cohesive strength to resist gravitational collapse of the scarp. In addition, simple collapse scarps occur in cases where the sediment has insufficient strength to resist gravitational collapse and instead form large tensile fractures with colluvium deposited at the base of the scarp (Fig. 2f). The 2016 M 7.8 Kaikoura, New Zealand rupture featured simple and simple collapse scarps with the along-strike variability observed at this site (Fig. 2f) (Nicol et al., 2018).

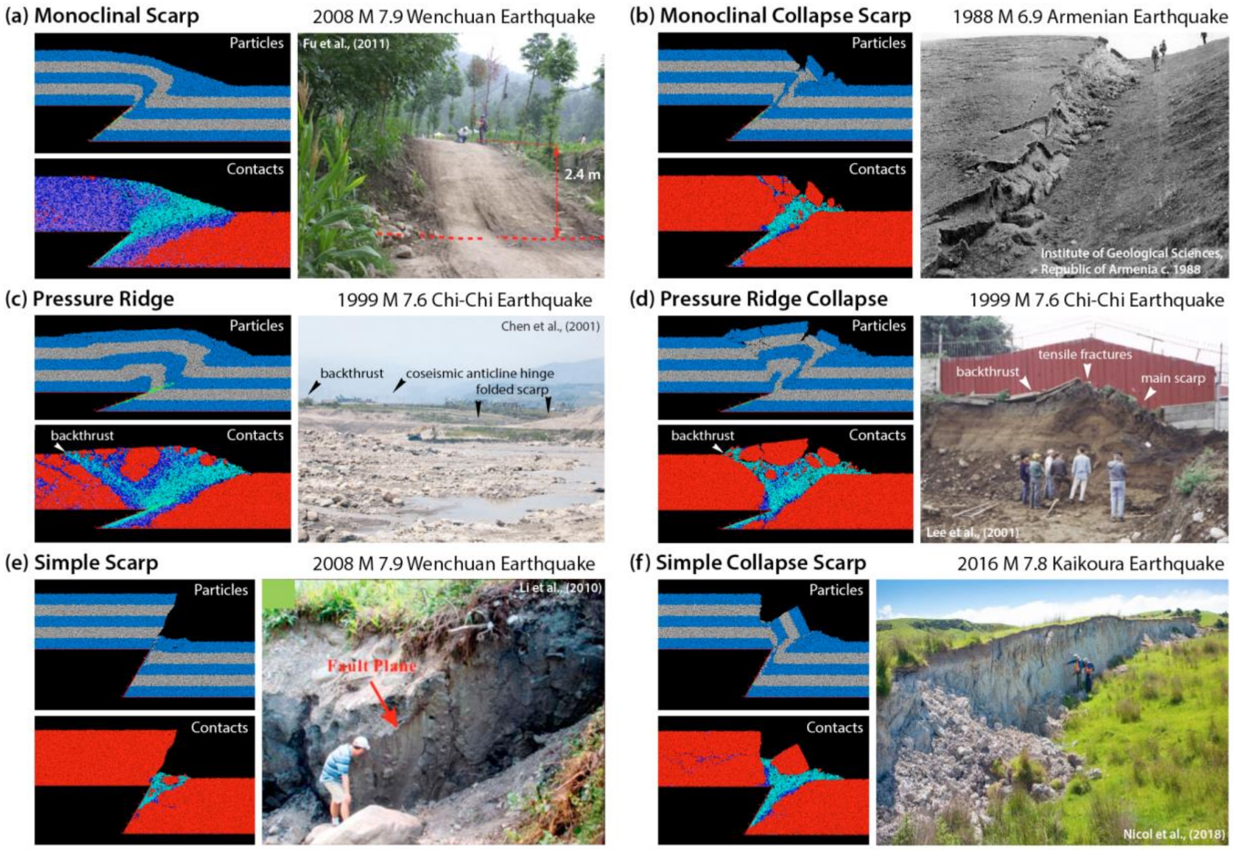

Fig. 2. Summary of the different scarp type morphologies as proposed in Chiama et al. (2023) comparing 2D DEM models of homogeneous sediment strengths. (a) Monoclinal Scarps (b) Monoclinal Collapse Scarps (c) Pressure Ridge Scarps (d) Pressure Ridge Collapse Scarps (e) Simple Scarps (f) Simple Collapse Scarps.

In this study, we present a total of 2,459 homogeneous, and 975 heterogeneous sediment experiments in a 2D DEM model to consider a wide range of possible earthquake ruptures across all scarp classes. We evaluate the surface deformation characteristics (deformation zone width, vertical scarp displacement, and scarp dip) of these models using computer vision techniques based on computer vision techniques such as image masking, signal processing, and specialized feature extraction tailored to the specific scarp types. We present a statistical analysis based on these characteristics and describe relationships between the accumulation of slip on the fault (relative to the magnitude of an earthquake), the sediment depth, the influence of the fault dip, and the impact of the sediment strength on the pattern of surface fault ruptures. We propose that this data that can be used to inform both probabilistic and deterministic approaches to assessing ground rupture hazards.

METHODS

The distinct element method (DEM) is a useful numerical modeling tool that generates individual particles that impart forces, interact with each other with translational or rotational motion, have linear spring behavior in compression, feature Coulomb frictional sliding in shear, and can be ascribed with different contact bonds to model a range of rheological or material properties (Itasca, 1999; Hughes et al., 2014; Chiama et al., 2023; Benesh and Shaw, 2023).

DEM is commonly used to investigate processes in Earth Sciences and has been applied to many questions in structural geology and active tectonics, including: the formation of fault gouge in shear zones (Mora and Place, 1998, 1999; Morgan, 1999, 2004; Morgan and Boettcher, 1999; Guo and Morgan, 2004; Egholm et al., 2008), thin-skinned thrust-fault evolution (Strayer and Hudleston, 1997; Strayer and Suppe, 2001; Strayer et al., 2004; Benesh et al., 2007), extensional faulting and folding (Finch et al., 2004; Egholm et al., 2007), and gravitational collapse of volcanic edifices (Morgan and McGovern, 2005a, 2005b). Efforts to investigate fault-related folding have focused on detachment folding (Hardy and Finch, 2005), basement-involved thrust and fault-propagation folding (Strayer and Suppe, 2001; Finch et al., 2003; Hardy and Finch, 2006, 2007; Hughes et al., 2014; Hughes and Shaw, 2015), fault-bend folding (Erickson et al., 2001, 2004; Strayer et al., 2004; Benesh et al., 2007; Benesh and Shaw, 2023), as well as fold-and-thrust belt and accretionary wedge mechanics (Strayer et al., 2001; Naylor et al., 2005; Morgan, 2015; Hughes, 2020). DEM modeling is particularly well suited to describing fault scarp formation, as it can effectively reproduce fault displacements at depth and the granular mechanics of shallow sediment deformation (Garcia and Bray, 2018a, 2018b; Chiama et al., 2023). More information on the methodology can be found in (Chiama et al., 2023 and the Supplemental Material).

MODEL GEOMETRY AND FORMATION

We developed 2D DEM models in Particle Flow Code 2D (PFC2D: version 7.00) by Itasca (1999, 2021) based on the initial work of Cundall and Strack (1979). The DEM model workflow includes 3 main stages in which we (1) generate the sediment assemblage by defining the density and sediment depth, (2) define sediment strength mechanics, and (3) define the faulting parameters before inducing slip in the model to simulate deformation.

We generated sediment assemblages in the DEM model that consist of dense, medium-dense, and loose sediment each across a range of three depths (3, 5, and 10 m), for a total of nine assemblages. These assemblages were constructed using the method presented by Garcia & Bray (2018a) in which the initial friction coefficient (μ_{int}) is modified during the gravitational settling of particles to form a denser or looser packing of particles. The resulting porosity and void ratio of the sediment assemblages is reported in Table 1.

Table 1. DEM Sediment Assemblage Properties.

Sediment Assemblage	μ_{int}	Porosity	Void Ratio
Dense	0	0.15	0.18
Medium	0.25	0.17	0.21
Loose	0.5	0.19	0.23

Next, we bonded the particles using the parallel-bond contact model provided by Itasca (1999). This contact bond simulates a cement between particles and provides cohesion and tensile strength that can be modified to simulate a range of sediment strengths. Values of cohesion and tensile strength less than 1.0 MPa are considered ‘weak’ whereas values greater than 1.0 MPa are considered ‘strong’ (Chiama et al., 2023). We performed numerous biaxial stress tests to compare DEM micro-properties to representative bulk scale rheologies of soil and sediment. The representative values for Young’s Modulus (E), failure angle (θ), friction angle (φ), and measured bulk friction coefficient (μ_{bulk}) for each of the sediment assemblage densities and contact bond strengths is reported in Table 2.

Table 2. DEM Parameters & Measured Bulk Material Properties.

Sediment Assemblage	Contact Bond Strength (coh = ten; MPa)	Young's Modulus (MPa)	θ (º)	φ (º)	μ_{bulk}
Dense	0.1	8.83	62.0	34.0	0.68
	0.5	11.99	63.5	37.0	0.75
	1.0	14.02	60.0	30.0	0.58
	1.5	16.72	60.0	30.0	0.58
	2.0	17.43	61.0	32.0	0.63
Medium	0.1	14.08	60.0	30.0	0.58
	0.5	18.38	63.0	36.0	0.73
	1.0	20.29	63.5	37.0	0.75
	1.5	20.44	61.7	33.3	0.66
	2.0	20.42	63.8	37.5	0.77
Loose	0.1	16.92	64.0	38.0	0.78
	0.5	19.42	63.5	37.0	0.75
	1.0	21.57	62.8	35.5	0.71
	1.5	22.73	62.3	34.5	0.69
	2.0	23.44	64.0	38.0	0.88

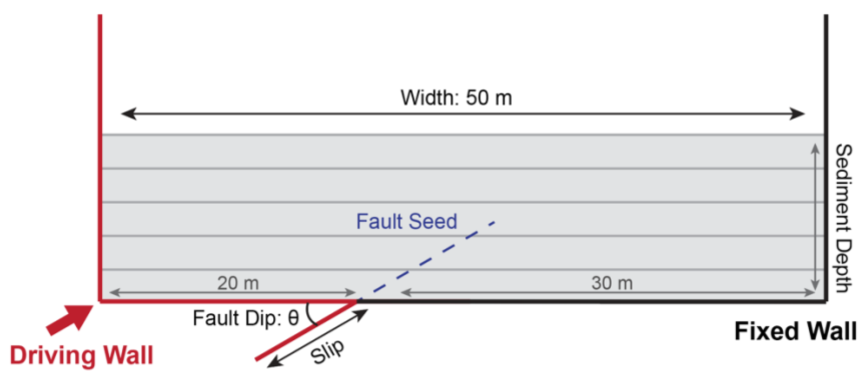

Fig. 3. DEM model geometry and boundaries (not to scale) modified from Chiama et al., (2023).

The model geometry (Fig. 3) is similar to analog sandbox fault models such as Cole & Lade (1984), Bransby et al. (2008), and Garcia & Bray (2018a,b) such that deformation is driven by displacement boundary conditions. We evaluated a range of fault dip (θ) angles (20º, 30º, 40º, 45º, 50º, 60º, and 70º) to represent many cases of naturally occurring thrust and reverse fault earthquakes. We slip the model from 0 to 5 m at a rate of 0.3 m/s. We use a timestep of 3E-05 s which yields 9E-06 m of displacement in each timestep. The slip rate of the models is within the lower range expected for coseismic fault displacements at depth. We found that higher slip rates in our models yielded unrealistic phenomena that resulted from the iterative force balance process inherent in DEM.

Prior to the initiation of slip, we defined a 'fault seed' in the model that represents a plane of weakness at the prescribed fault dip at depth (Fig. 3). The fault seed localizes deformation to the defined slip plane at the base of the model and prevents undesirable boundary condition issues. Furthermore, it represents a case where the fault has ruptured previously and developed fault gouge weaker than the surrounding material. We evaluated a range of cases where the tip of the fault (vertical height of the fault seed) is buried by a range of sediment depths to evaluate how the fault will propagate through unruptured sediment. The length of the fault seed function is a fraction of the total sediment thickness by the fault dip angle. The total length of the fault seed (L) for each model is calculated as follows in Equation 1:

$$L = \frac{H \cdot F}{sin(\theta)} \tag{1}$$

where H is the total sediment thickness, F is a fraction of the total sediment thickness, and θ is the fault dip angle. Given sediment depths of 3, 5 and 10 m, we tested cases where the fault seed is 25%, 50% and 75% of the total sediment depth. Equation 1 standardizes the unruptured sediment above the fault tip across different fault dips. For example, a shallow fault of 20º will have the same amount of unruptured sediment above the fault tip as steeper faults of 70º. Therefore, we consider a fault tip buried by 0.75, 1.25, 1.5, 2.25, 2.5, 3.75, 5, and 7.5 m of unruptured sediment for depths of 3, 5, and 10 m. See Chiama et al. (2023) for more information.

We evaluated both homogeneous and vertically heterogeneous sediment strengths in our experiments. For the homogeneous experiments, we tested contact bond strengths of cohesion equal to the tensile strength (0.1, 0.5, 1.0, 1.5, 2.0 MPa), cohesion set to a standard value of 1.0 MPa while the tensile strength varies, and tensile strength set to a standard value of 1.0 MPa while the cohesion varies. This yielded a total of 13 combinations of homogeneous sediment strengths for a total of 2,459 DEM experiments.

For the heterogeneous experiments, we tested three cases for each of the nine sediment assemblages: a weak (0.1 - 1.0 MPa), moderate (0.5 - 1.5 MPa), and strong (1.0 - 2.0 MPa) case for a total of 567 experiments. Each sedimentary layer is standardized to 1 m thick with the base of the model defined as the strongest unit and weakening towards the surface by set intervals. By standardizing the layer thickness with respect to the sediment strength, we can evaluate how sediment depth may impact the resultant ground surface morphology. The values for the heterogeneous sediment strengths are defined in Table 3. Additionally, we tested three specified suites of heterogeneous sediment layers: 1) a one-meter cohesive top unit above moderate (1.0 MPa) strength sediment; 2) 10 sets of randomized sediment strengths; and 3) alternating layers of strong and weak (2.0 MPa and 0.1 MPa) strengths. First, we evaluated a case study on the impact of a cohesive top unit on sediment depth (3, 5, and 10 m profiles), density (dense, medium-dense, loose), fault dip (20º - 70º), and unruptured sediment above the fault tip for a total of 189 experiments. Next, we tested a case study of randomized heterogeneous sediment strengths. We generated 10 non-repeating sets of cohesive strength from 0.1 to 2.0 MPa in 0.1 MPa increments using a random number generator. We varied the strength in each 1 m unit layer for dense, 10 m deep sediment based on the set of 10 randomly generated numbers (these values are reported in Supplemental Table 1). The randomized sediment was applied in a dense, 10 m deep sediment profile and evaluated across all fault dips (20º - 70º) and unruptured sediment above the fault tip depths for a total of 210 experiments. Finally, we tested a case study alternating sediment strengths in a dense, 10 m deep profile and tested on fault dips of 20º, 40º, and 60º and all unruptured depths above the fault tip for a total of 9 experiments.

Table 3. Heterogeneous Sediment Strength 2D DEM Experiments.

Sediment Depth (m)	Sediment Type	Sediment Name	Cohesion and Tensile Strength Values (top to bottom of model; MPa)

3	Weak	A	0.1, 0.5, 1.0
	Moderate	B	0.5, 1.0, 1.5
	Strong	C	1.0, 1.5, 2.0
	Cohesive Top Unit	Q	2.0, 1.0, 1.0
5	Weak	F	0.1, 0.25, 0.5, 0.75, 1.0
	Moderate	G	0.5, 0.75, 1.0, 1.25, 1.5
	Strong	H	1.0, 1.25, 1.5, 1.75, 2.0
	Cohesive Top Unit	Q	2.0, 1.0, 1.0, 1.0, 1.0
10	Weak	K	0.1, 0.2, 0.3, 0.4, 0.5, 0.6, 0.7, 0.8, 0.9, 1.0
	Moderate	L	0.6, 0.7, 0.8, 0.9, 1.0, 1.1, 1.2, 1.3, 1.4, 1.5
	Strong	M	1.1, 1.2, 1.3, 1.4, 1.5, 1.6, 1.7, 1.8, 1.9, 2.0
	Cohesive Top Unit	Q	2.0, 1.0, 1.0, 1.0, 1.0, 1.0, 1.0, 1.0, 1.0, 1.0

SURFACE DEFORMATION CHARACTERISTICS DATASET

We constructed a dataset of the DEM model input parameters (model geometry, particle size, sediment depth, sediment density, sediment strength, fault dip, fault seed depth, fault slip, estimated earthquake magnitude) as well as resultant ground surface deformation characteristics.

The DEM experiments generated a PNG image every 500 cycles of the deformation sequence (representing 0.0045 m of slip on a fault), resulting in ~1,114 images for each experiment. Considering the size of the homogeneous (2,459) and the heterogeneous (975) DEM experiments (~3.85 million images in total), it was necessary to employ a computer vision (CV) model in order to efficiently process the images and extract meaningful data from them (Chiama et al., 2024a). The CV model was tailored to specific features in the images of DEM model experiments which correspond to measurements of surface ruptures that would be obtained in the field after a large earthquake (scarp height, uplift, deformation zone width, and scarp dip). By leveraging this geological perspective, our DEM measurements are able to be directly compared to field measurements of historic earthquakes (e.g., FDHI dataset, Sarmiento et al., 2021).

We used the CV model to examine the DEM experiments at intervals of 0.05 m of slip, yielding 101 measurements (from 0 to 5 m of slip) of each DEM model with a total of 248,263 measurements of homogeneous sediment models and 98,475 measurements of heterogeneous sediment models. The 0.05 m of slip interval was chosen because it is computationally efficient but still is temporally resolved enough to capture the progression of the surface rupture. Further, it ensures that the measurements of the DEM models are unique rather than oversampling the dataset. Chiama et al. (2024a) discusses the application of the CV model on a training dataset comprised of the 45 DEM models presented in Chiama et al. (2023) and illustrates the improved ability of the CV model to collect measurements of ground surface deformation at a significantly higher resolution than Chiama et al. (2023) as well as classify each of the scarp types based on their current stage rather than the end-stage result of the DEM model.

The CV model was constructed based on multiple machine learning software packages to interpret the DEM model images (Hunter, 2007; Pendregosa et al., 2011; Walt et al., 2014; Clark, 2015; Harris et al. 2020; Van Rossum, 2020). First, the CV model preprocesses the image, smoothing out noise and extracting the topographic surface. By extracting the surface, we can use one-dimensional signals to identify certain features present on the surface. Such features include uplift from the hanging wall which indicates a pressure ridge, or a flattening of the scarp towards the footwall which indicates the end of the deformation zone. Second, we extract the side profile of the scarp to pick out the distinctive “Z” shape associated with the direct fault displacements of simple scarps. We do not include the colluvium at the base of the simple scarps in the calculation of scarp dip. Finally, our model also uses object detection to aid in finding blocks of colluvium which may have broken off in order to determine if a scarp has collapsed. After the extraction of these points, the CV model then is able to classify the scarp type and derives surface deformation measurements. Measurements were obtained using pixel dimensions converted to meters using the ratio of pixels to the hanging wall depth.

There are four ground surface deformation characteristics that we measure from the DEM models: scarp height (U_s), additional uplift (U_s - U_d), deformation zone width (DZW), and scarp dip (Fig. 4). The scarp height (U_s) is measured as the total scarp height from the top of the undeformed footwall block. In cases where there is a pressure ridge, the scarp height exceeds the undeformed surface of the hanging wall due to folding and uplift from secondary faults or backthrusts. Therefore, we calculate the U_s - U_d from Chiama et al. (2023) where U_d is the uplift (or vertical displacement) on the fault at depth. The total scarp height is measured such that additional uplift above the top of the undeformed hanging wall yields a positive value of U_s - U_d whereas monoclinal or simple scarps will yield a near-zero value of U_s - U_d. The DZW is measured from the initial vertical displacement (uplift, tensile fractures, or collapse) observed in the hanging wall block to the base of the scarp in the footwall block. The scarp dip is measured from the maximum scarp height to the toe of the scarp as an angle from the horizontal. The dataset also reports an R^2 value to characterize the ground surface roughness related to the fit of the scarp dip to the rupture. This value is line-length balanced over the DZW to encompass cases such as the pressure ridge which has two scarp dips present (the backthrust and forethrust). Smooth models of surface ruptures will present a good-fit of the R^2 value whereas rougher ruptures with tensile fractures or large blocks of colluvium will present a poor-fit R^2 value.

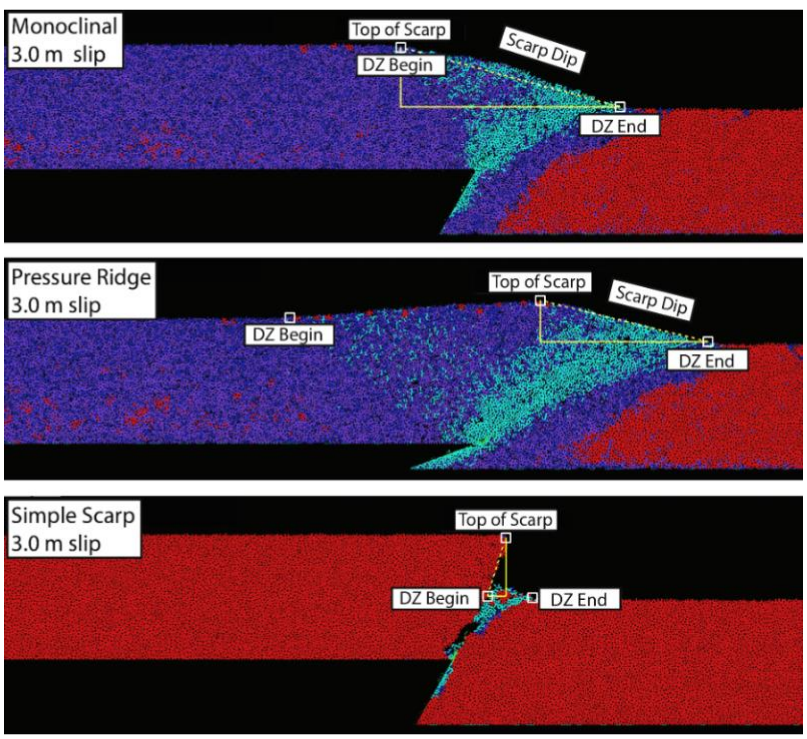

Fig. 4. Scarp classes (monoclinal, pressure ridge, and simple scarps) and the measurements obtained by the CV model for the top of the scarp, the deformation zone (DZ) beginning and ending points, and the scarp

dip. Models are shown as contact bonds between particles: red are bonded, dark blue are bonds broken in tension, dark purple are bonds broken in shear, light blue are entirely broken bonds.

The CV model cannot differentiate small displacements at the surface caused by the initial stages of fault slip from roughness (noise) in the ground surface due to the particle size distribution. Therefore, we applied a smoothing value to the surface rupture to capture the main displacements and remove surface roughness due to particle distributions. Nevertheless, given these limitations of the CV model to obtain ground surface measurements at low values of slip, we omitted measurements of high uncertainty in the dataset. This corresponds to negative values of the DZW where the average value of slip is 0.213 ± 0.098 m (count: 3488), scarp dips that defaulted to values of -90º (slip: 0.094 ± 0.055 m, count: 655), and scarp dips that are greater than 90º (slip: 0.14 ± 0.092 m, count: 5169). This corresponds to 9,312 measurements (or 2.7% of the dataset) that were below the minimum threshold to be successfully measured by the CV model.

Since the DEM model is driven by the accumulation of slip on the fault at depth, we can relate our measurements to earthquake magnitude. We estimate the approximate magnitude of an earthquake based on the empirical relationships of Biasi and Weldon (2006):

$$M = 6.94 + 1.14 \cdot log(d_{ave}) \tag{2}$$

where *M* is the magnitude of an earthquake and d_{ave} is the average displacement. We consider the slip on the fault in our DEM models as the average displacement of an earthquake. Our DEM models evaluate slip ranges from 0.05 m to 5.0 m which corresponds to a range of earthquake magnitudes of M 5.46 to 7.74.

RESULTS & DISCUSSION

This section reports the results of our homogeneous and heterogeneous sediment experiments. We compare the data between scarp types within each subset of experiments and then report the results of the entire dataset. We discuss relationships between input DEM parameters and surface deformation characteristics (scarp height, deformation zone width, and scarp dip). Finally, we perform a case study analysis of how this dataset can be used to forecast ground surface deformation features by comparing it to the 1952 M 7.36 Kern County, CA earthquake.

HOMOGENEOUS SEDIMENT RESULTS

Our first model suite consists of 2,459 homogeneous sediment DEM experiments and their resultant ground surface deformation characteristics. Given that these models were assessed at increments of 0.05 m displacement up to 5.0 m of total displacement, the full suite of data includes 248,359 model states where measurements were obtained. This dataset is available open-access on DesignSafe (Chiama et al., 2024b). These data are plotted by the surface rupture characteristics and the accumulation of slip on a fault at depth as well as estimated earthquake magnitude in Figure 5. Each datapoint is colored by its scarp classification type as defined by Chiama et al. (2023). We observe that each scarp type has a unique set of ground surface deformation characteristics and tends to form unique clusters (Fig. 5).

The scarp heights across all experiments trend upwards with increasing accumulation of slip on a fault. There is a near-linear relationship for the amount of vertical displacement on the fault at depth and the total scarp height for monoclinal, monoclinal collapse, simple, and simple collapse scarps. This is reflected by the near-zero values of U_s - U_d (Fig. 5a,c). In contrast, the pressure ridge and pressure ridge collapse scarps attain higher values of total scarp uplift than the amount of vertical displacement at depth based on the highly positive values of U_s - U_d (Fig. 5a,c). These relationships are similar when plotted by the estimated magnitude of an earthquake from Biasi and Weldon (2006), however, scarp height and U_s - U_d are exponential (Fig. 5b,d). Therefore, higher magnitude earthquakes will have increasingly higher scarp heights.

The deformation zone width (DZW) has a wide range across all the experiments (0 - 40.76 m). The DZW for simple and simple collapse scarps is the smallest, while monoclinal and pressure ridge scarps have substantially wider DZWs at similar values of fault slip (Fig. 5e,f). The pressure ridges have the widest DZW due to the formation of backthrusts. Effectively, the primary fault (forethrust) and backthrust define a broad zone of uplift and deformation yielding a wider scarp than monoclinal and simple scarp types. As noted, pressure ridge scarps also have positive values of U_s - U_d, indicating heightened uplift between the fore- and backthrust.

The scarp dip is separated into two main groups, defined by the presence of a scarp overhang (Fig. 5g,h). The monoclinal, monoclinal collapse, pressure ridge, and pressure ridge collapse scarps have scarp dips which increase with slip at depth until they reach the angle of repose, at which point the scarp dip measurements become near-constant (Fig. 5g). The simple-related scarps are defined by direct fault displacements or scarp overhangs. Therefore, simple scarp measurements show generally higher dips than other scarp types (Fig. 5g,h). Notably, there are no simple scarps present in the dataset until ~1 m of slip accumulates on the fault at depth (~ M 7.0 earthquake; Biasi & Weldon, 2006). This is expected since simple scarps are not often observed in nature, and if they do occur, they are the result of a large magnitude earthquake with surface rupture in strong (highly cohesive) sediments. For example, 2008 M. 8.0 Wenchuan, China (Li et al., 2010) and 2016 M 7.8 Kaikoura, New Zealand (Nicol et al., 2018) earthquakes produced simple and simple collapse scarps respectively (Chiama et al., 2023).

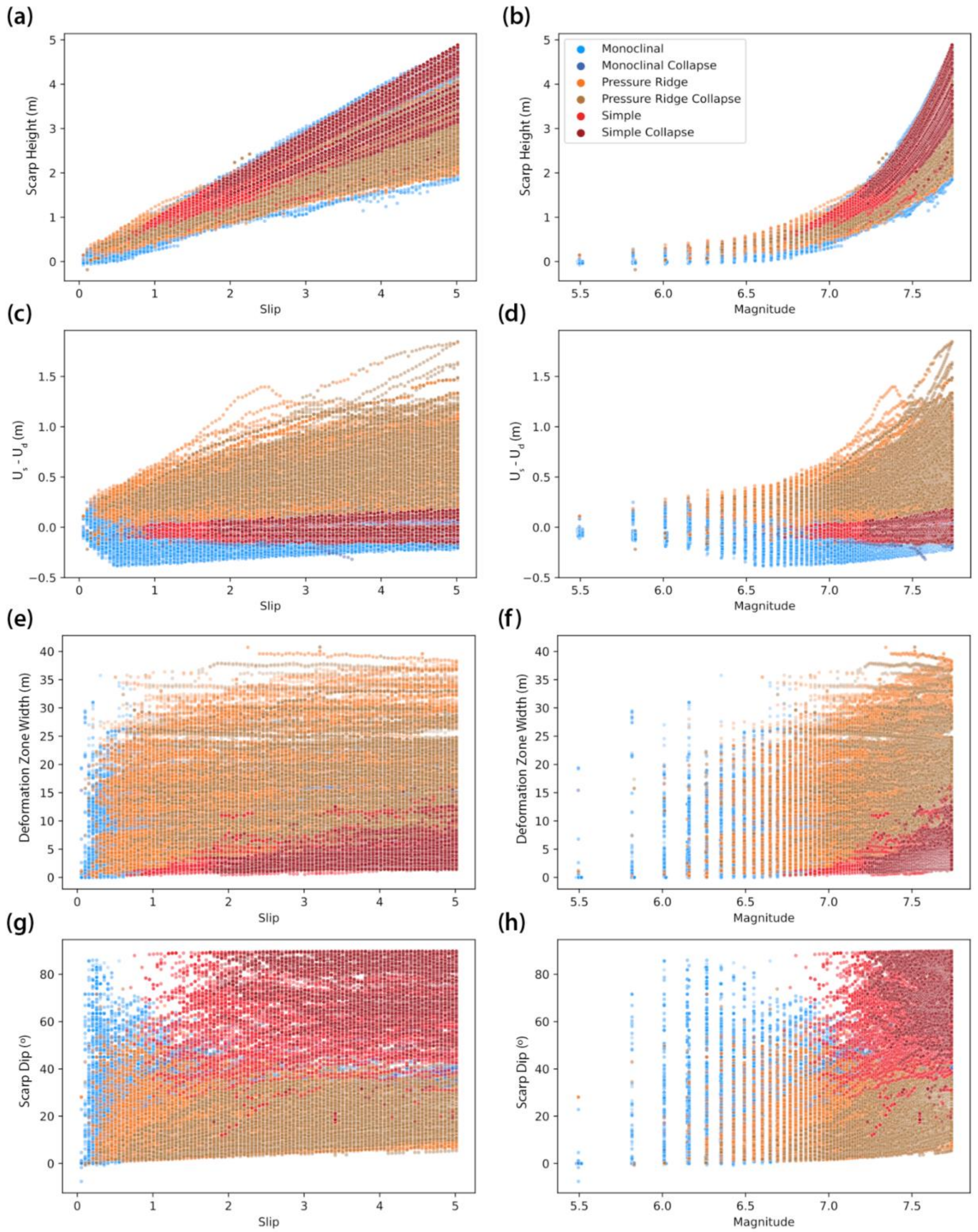

Fig. 5. Plot of the scarp characteristics (scarp height, U_s - U_d deformation zone width, and scarp dip) for homogeneous experiments by the accumulation of slip on a fault at depth (*left*) and the estimated magnitude of an earthquake (*right*) based on the empirical relationships of Biasi and Weldon (2006). Monoclinal scarps are in blue, pressure ridge in orange, and simple scarps in red. Note that many of the monoclinal scarp

measurements (blue) are plotted underneath other measurements (Fig. 5). Full plots of individual scarp classes are provided in the Supplemental Material (Fig. S2 – 7).

GENERAL HETEROGENEOUS SEDIMENT RESULTS

Next, we discuss the results of the 975 heterogeneous sediment DEM experiments and their resultant ground surface deformation characteristics. The full suite of data (98,475 measurements, Chiama et al., 2024c) is plotted by the surface rupture characteristics and the accumulation of slip on a fault at depth as well as estimated earthquake magnitude in Figure 6. Similar to the homogeneous results, each datapoint is classified by its scarp type as defined by Chiama et al. (2023). Once more, we observe that each scarp type has a unique set of ground surface deformation characteristics and tends to form unique clusters, although there is more variability present in the heterogeneous data compared with the homogeneous data in specific parameters (Fig. 6).

The scarp height measurements (Fig. 6 a,b,c,d) follow similar trends to the homogeneous measurements. There is a direct relationship between the amount of vertical displacement on a fault at depth and the total scarp height. Simple scarps tend to reach the highest scarp heights whereas pressure ridges feature lower overall scarp heights but yield positive values of U_s - U_d, indicating additional uplift between the fore- and backthrust above the top of the undeformed hanging wall. There is little evidence that heterogeneous sediment mechanics impacts the scarp heights present in the dataset.

The DZW measurements of the heterogeneous data show more variability than the homogeneous results, especially at the onset of slip. This may be due to heterogeneous sediment strengths causing more complexity in the strain patterns at low displacements which yields more variability in surface scarp patterns. This is further impacted by limitations of the CV model to measure scarp parameters at low slip, as previously discussed in the Methods section (Fig. 6 e,f). Nevertheless, the same trends are present such that the pressure ridges have the widest DZW throughout the accumulation of slip and the simple scarps have the smallest DZW.

However, there is a limitation on the total DZW in heterogeneous sediment profiles. While some homogeneous models of pressure ridges easily reach 30 to 40 m DZW, the heterogeneous cases have a DZW limited to ≤ 30 m DZW. This indicates that there is a component of sediment strength that impacts the total DZW. As the fault propagates to the surface in pressure ridge models, the DZW is defined by the extent of the backthrust to the forethrust. In weaker sediment models, the fault will propagate to the surface along a shallower plane and thus create a wider DZW. In stronger sediment, the fault propagates up at a steeper angle and thus generates a smaller DZW. Therefore, we suggest that the lower values of DZW in heterogeneous models is due to the strength contrasts between sediment layers. Effectively, the stronger layers in heterogenous models limit the DZW from achieving the largest values observed in the weakest homogeneous sediment models.

Regarding the scarp dip of the heterogeneous experiments, there is a very similar distribution of scarp dip over the accumulation of slip to the homogeneous experiments (Fig. 6 g,h). The monoclinal, monoclinal collapse, pressure ridge, and pressure ridge collapse scarps all feature increasing values of scarp dip as they reach the angle of repose of the sediment. The simple and simple collapse scarps both feature steep scarp dips representing direct fault displacements and scarp overhangs.

HETEROGENEOUS CASE STUDIES

This section will briefly discuss the overarching patterns observed in the heterogeneous case studies, additional plots are included in the Supplemental Material (Fig. S8 – S13).

The heterogeneous vertical gradients vary each sedimentary layer (standardized to one-meter thick) from weak, moderate, strong sediment strengths across all sediment densities and depths for a total of 567 experiments. The weak sediment profiles mainly feature monoclinal or pressure ridge scarps with positive values of U_s - U_d and the widest DZWs with scarp dips around the angle of repose (Fig. S8). The moderate strength sediment gradients are also predominately monoclinal or pressure ridge scarps but start to develop some cases of simple scarps with steep scarp dips (Fig. S9). Finally, the strongest sediment gradients are largely characterized by the collapse-modified pressure ridge and monoclinal scarps as these experiments tend to develop tensile fractures and distinct blocks of colluvium (Fig. S10). There is also a larger proportion of simple and simple collapse scarps that develop in these cases. Overall, the strongest sediment gradients feature lower overall DZWs and steeper scarp dips than the weak and moderate cases.

Next, we consider the 210 experiments in which we applied randomized sediment strengths in dense, 10 m thick profiles (Fig. S11). There is more variability in these experiments than the vertical sediment gradients, however, there are predominately monoclinal, monoclinal collapse, pressure ridge, and pressure ridge collapse scarps that develop with a few rare cases of simple or simple collapse scarps. Overall, there are positive values of U_s - U_d, wide DZWs, and scarp dips near the angle of repose with a few steep simple and simple collapse scarp dips.

Finally, we consider the 189 experiments that feature a cohesive top unit above moderately strong sediment (Fig. S12). This set of experiments tends to develop tensile fractures and rough ground surface deformation due to the localization of shear to distinct bands within the top-most cohesive unit. The localized fault splays form distinct blocks of colluvium that dominates the general morphology of ground surface deformation. Thus, these experiments are predominately collapse-modified versions of the scarp types and feature a large proportion of simple and simple collapse scarps. In summary, there are positive values of U_s - U_d and wide DZWs for the pressure ridge collapse scarps as well as highly variable scarp dips from the angle of repose to steep scarp overhangs due to the additional ground surface roughness. The distributions of these measurements are most similar to the strongest vertical sediment gradients.

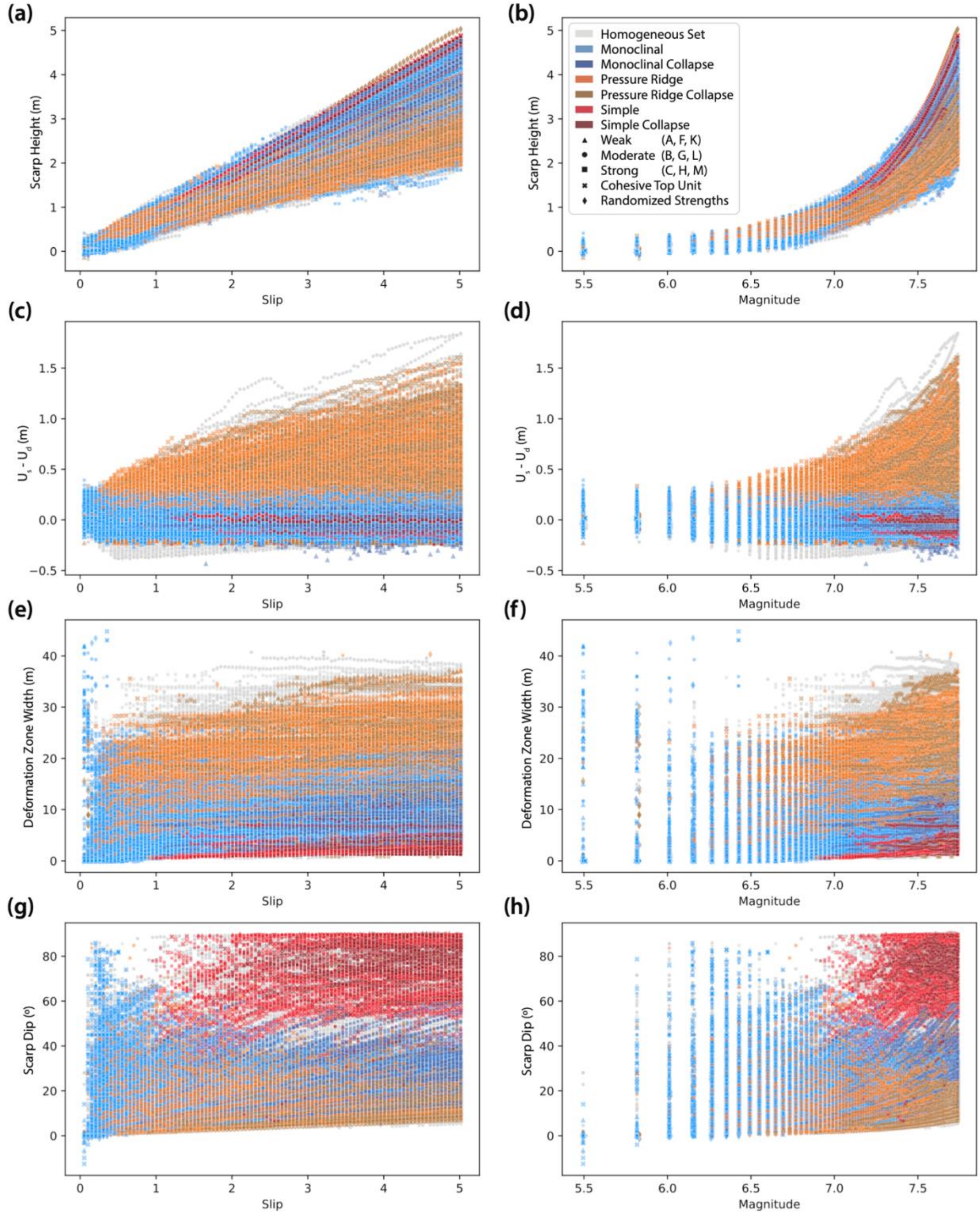

Fig. 6. Plot of the scarps characteristics (scarp height, U_s - U_d deformation zone width, and scarp dip) for heterogeneous experiments by the accumulation of slip on a fault at depth (left) and the estimated magnitude of an earthquake (right) based on the empirical relationships of Biasi and Weldon (2006). Homogeneous dataset in light grey. The different groups of sediment strength case studies are plotted with different

markers and many of the measurements are overlaid on top of each other. Individual heterogeneous sediment plots are included in the Supplement (Fig. S8 – 13).

FULL MODEL DATASET

Combining the homogeneous and heterogeneous models, we performed a total of 3,434 DEM experiments considering the sediment depth, density, sediment strengths, fault dip, and the amount of unruptured sediment above the fault tip. There are a total of 346,834 model stages taken every 0.05 m of slip with measurements of ground surface deformation characteristics (scarp height, U_s - U_d, DZW, and scarp dip). This dataset is available open-access on DesignSafe (Chiama et al., 2024b,c; doi: 10.17603/ds2-gfsj-pp60, doi: 10.17603/ds2-xpq0-gw80). A summary of this data is presented in Figure 7 plotted by the mean ± σ (standard deviation) for each scarp type. The distribution for each of the surface deformation characteristics organized by scarp class is shown in Figure 8. The supplemental material contains Tables S2 – S11 which report the n-value, mean, median, standard deviation, minimum and maximum values of each group of data in Figures 7 – 11 as well as lines of best fit for the mean scarp type measurements in Figure 7.

Monoclinal scarps are the most prevalent in the dataset (51.3% or 178,036 unique counts, Fig. 8). This is because all scarps originate as monoclinal at the initiation of slip on a fault at depth. Once enough slip has accumulated, different morphology characteristics may develop (i.e., backthrusts for pressure ridges, fault scarp overhangs for simple scarps) that reclassify the scarp type. Additionally, there must be enough vertical displacement on the fault at depth to initiate gravity-driven hanging wall collapse for the collapse-modified scarps. Pressure ridge scarps are the second most prevalent (16.2% or 56,150 counts) followed by monoclinal collapse (12.3% or 42,752 counts), pressure ridge collapse (7.5% or 25,873 counts) and simple (5.2% or18,058 counts). Simple collapse scarps are the least common in the dataset with only 3.5% or 12,290 counts. However, we anticipate that in nature after coseismic ruptures, most simple scarps would degrade to form simple collapse scarps over time.

The monoclinal, monoclinal collapse, simple, and simple collapse scarps have a near-linear relationship of mean scarp height and the amount of slip at depth (Fig. 7a,b,c,d). This indicates that the scarp height is dependent on the vertical displacement on the fault at depth. Further, there is increasing variability in the standard deviation with increasing slip at depth. In contrast, the pressure ridge and pressure ridge collapse scarps have lower overall scarp heights but high values of U_s - U_d such that they attain significant uplift above the undeformed surface of the hanging wall. This is due to backthrusts and the internal folding that occurs in the hanging wall that increases the DZW of these scarps. Pressure ridge scarps tend to form in models with low prescribed fault dips (i.e., 20º or 30º) that are less than the internal friction angle of the sediment (~32.6º). The causes upward steepening of the primary fault causing a concentration of stress at the fault bend that localizes the formation of a backthrust. Once the backthrust forms, the scarp height is dependent on the amount of horizontal shortening that contributes to additional uplift above the surface of the hanging wall.

There is a general relationship of increasing DZW with the accumulation of slip for all scarp types (Fig. 7 e,f). Monoclinal and monoclinal collapse scarps form a triangular wedge of shear where the scarp height is related to the vertical displacement at depth. Therefore, the DZW of monoclinal and monoclinal collapse scarps increases with slip. Pressure ridge scarps also show a direct correlation between DZW and slip. This reflects that the DZW is defined by the scarps associated with the fore- and backthrusts, each of which is a monoclinal scarp that grows in width with increasing slip. The fore- and backthrusts form a triangular zone of deformation propagating from the tip of the fault seed up to the surface to form the pop-up structure. Therefore, the pressure ridge scarps have the highest values of uncertainty as their DZW is directly related to the unruptured sediment depth above the fault seed. Ergo, shallow experiments in 3 m of sediment will have smaller DZWs while deeper 10 m sediment has the widest possible DZWs. Regarding simple and simple collapse scarps, the scarp overhangs do not form until ~0.75 m and ~1.85 m of slip respectively. Once these features develop, the DZW is related to the horizontal displacement at depth and the process of hanging wall collapse attempting to maintain the angle of repose of the sediment.

The scarp dips show a limited relationship with the slip at depth (Fig. 7g,h). The monoclinal and pressure ridge scarps each show an increase in dip with fault displacement until they reach the angle of repose of the sediments. Thereafter, they maintain this dip angle with decreasing variance in the standard deviation and may transition to collapse type scarps. The simple scarps have a higher mean ± σ scarp dip (~ 60º - 70º) due to the direct fault displacements representing a scarp overhang. Overall, the collapse versions of the scarp types have higher variability in the mean ± σ scarp dip and often represent a steep (~75º) tensile fracture from which a large block of colluvium collapsed into the toe of the scarp. Further, the scarp dips of all classes feature an oscillatory pattern with increasing slip at depth. This is most pronounced for simple scarps and reflects that the scarps go through stages of growth and subsequent collapse once the angle of repose is exceeded.

We fit functions to each of these relationships based on scarp class for the scarp height, U_s - U_d, DZW, and scarp dip using a best-fit polynomial (Supplemental Table 11). These functions fit the averages of the data well with some scatter at the initiation of slip in the hanging-wall collapse modified versions of the scarps. There is some oscillation observed in the average values for the DZW and scarp dip. This is due to the scarps attempting to maintain the angle of repose. As the scarp height increases and exceeds the angle of repose, it will extend the DZW to maintain the angle of repose. Overall, we observe an increase in the scarp height, U_s - U_d, and DZW with additional slip on a fault at depth while scarp dip has two main groups: monoclinal and pressure ridge scarps maintain the angle of repose while the simple and simple collapse scarps have much steeper scarp dips. We anticipate that these trends continue for higher magnitudes of slip.

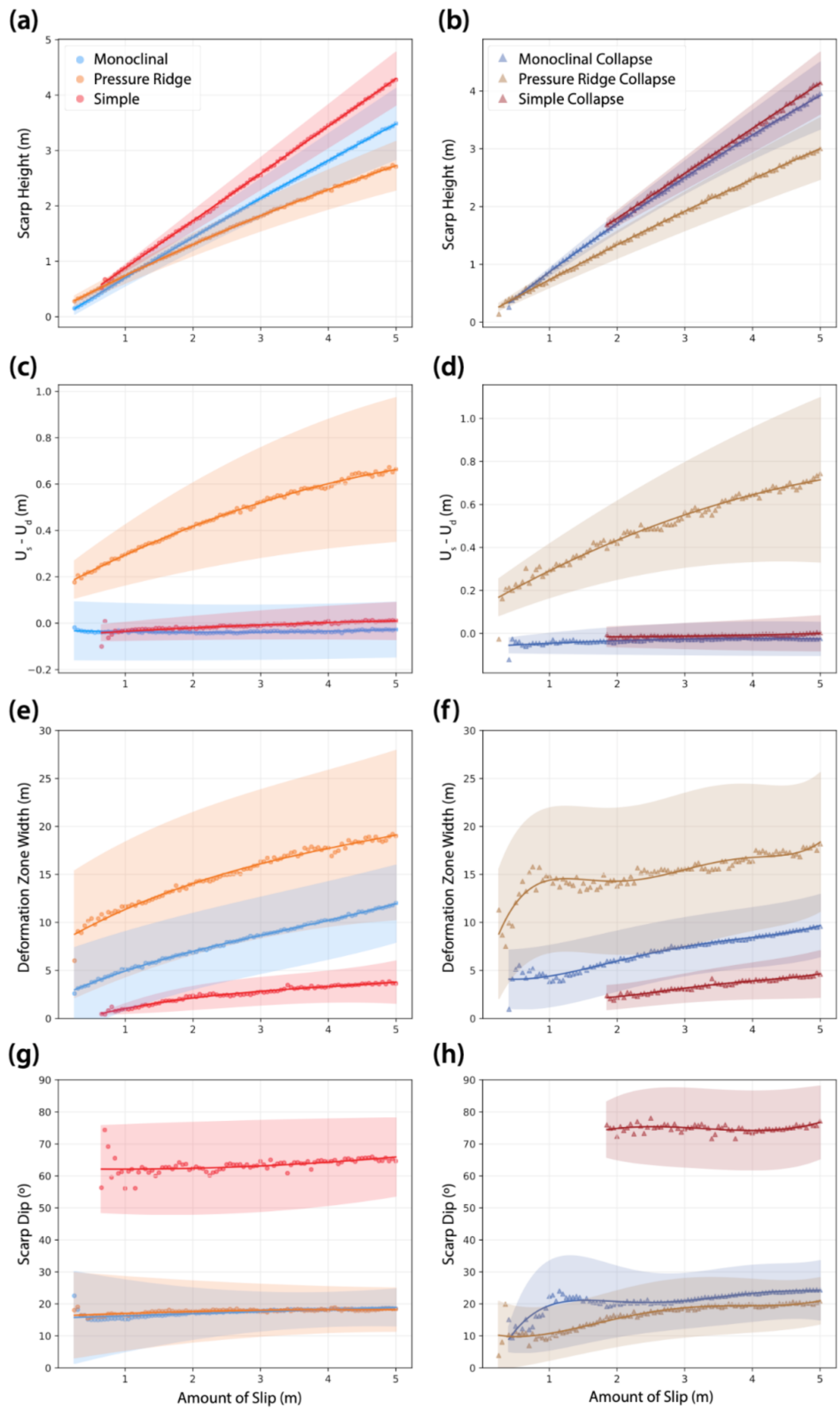

Fig 7. Averages and standard deviations for each of the surface deformation characteristics: scarp height, U_s - U_d, deformation zone width, and scarp dip organized by scarp class (monoclinal, pressure ridge, and simple scarps) and the hanging-wall collapse modified scarps.

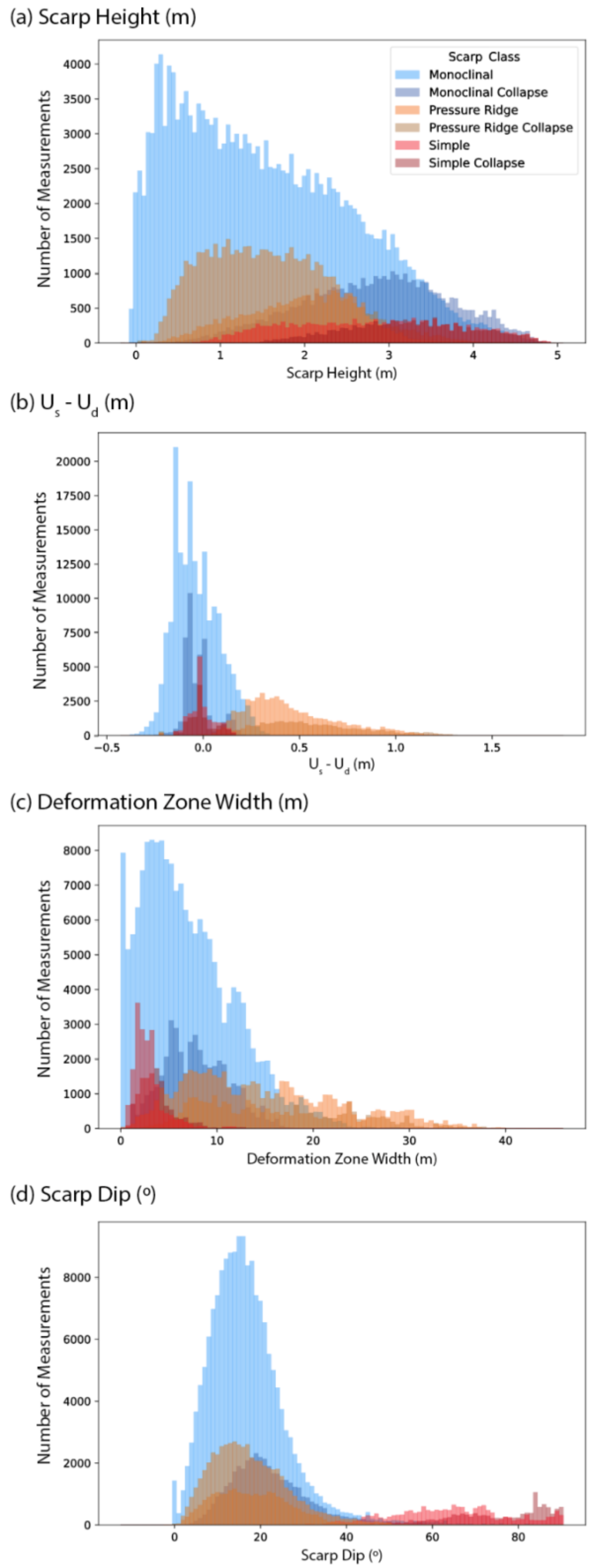

Fig. 8. Distributions of the measurements in the homogeneous and heterogeneous datasets organized by scarp class for each of the surface deformation characteristics: (a) scarp height, (b) U_s - U_d, (c) deformation zone width, (d) scarp dip.

FACTORS CONTROLLING SCARP CHARACTERISTICS

In the following sections, we present an analysis of the influence of individual DEM model parameters on the key measurements of ground surface deformation (scarp height, U_s - U_d, width [DZW], dip). Specifically, we consider the influence of the sediment depth, sediment strength, fault dip, and the amount of unruptured sediment above the fault tip on these scarp properties. Additional figures and correlation coefficient plots are included in the Supplemental Material as Figures S14 – S18.

We note that the homogeneous experiments evaluated 13 sediment strengths (0.1 – 2.0 MPa) in which we varied the cohesion and tensile strength of the contact bonds. However, we found that varying tensile strength had little impact on the model outcomes. Instead, changes in the cohesive strength yielded significant variability in ground surface deformation. Thus, in the following discussion we refer to the sediment strengths as weak (0.1 – 0.5 MPa), moderate (1.0 MPa), and strong (1.5 – 2.0 MPa) based solely on the cohesive strength of the contact bonds.

Scarp Height

Figure 9 depicts the distribution of scarp height and U_s - U_d by the scarp class and fault dip. Fault dip, and the resulting scarp class, has the most variation in the distribution of scarp heights while the sediment strength, density, depth, and fault seed depth do not impact the scarp height (See supplemental material for additional measurements).

Each of the scarp classes feature unique distributions of scarp height and U_s - U_d (Fig. 9a,b). Monoclinal scarps are the most frequent in the dataset as most models originate as a monoclinal scarp at the initiation of slip on a fault before enough slip has accumulated to transition to a pressure ridge, simple, or hanging wall collapse modified scarp. Monoclinal scarps have the lowest mean scarp heights (1.53 ± 1.04 m), closely followed by pressure ridge scarps (1.54 ± 0.71 m), while simple scarps have the highest mean scarp height (2.80 ± 0.98 m). Both monoclinal and simple scarps have near-zero values of U_s - U_d which suggests that the height of the scarp is dependent on the vertical displacement on a fault at depth. Meanwhile, pressure ridge scarps have a positive value of U_s - U_d (0.46 ± 0.25 m) which indicates that there is significant uplift beyond the undeformed surface of the hanging wall - likely due to secondary faulting, backthrusts, and folding.

The scarp height is directly related to the amount of vertical displacement at depth which is dependent on the amount of slip and the fault dip (Fig. 9e,f). Steep fault dips yield high fault scarps (70º: 2.38 ± 1.35 m) due to the vertical displacement of the hanging wall. There is a near-linear relationship between scarp height and the amount of vertical displacement at the surface on steep fault dips (e.g., > 45º; see values of U_s - U_d near 0 m in Fig. 9f). In comparison, shallow fault dips (e.g., < 45º) yield lower overall scarp heights (20º: 1.44 ± 0.72 m) and higher values of U_s - U_d (0.55 ± 0.30 m), which indicate a non-linear relationship with scarp height and vertical displacement at depth. The shallow faults tend to form pressure ridges with additional uplift above the top of the undeformed hanging wall. Thus, fault dip is the most influencing parameter on the resultant scarp height.

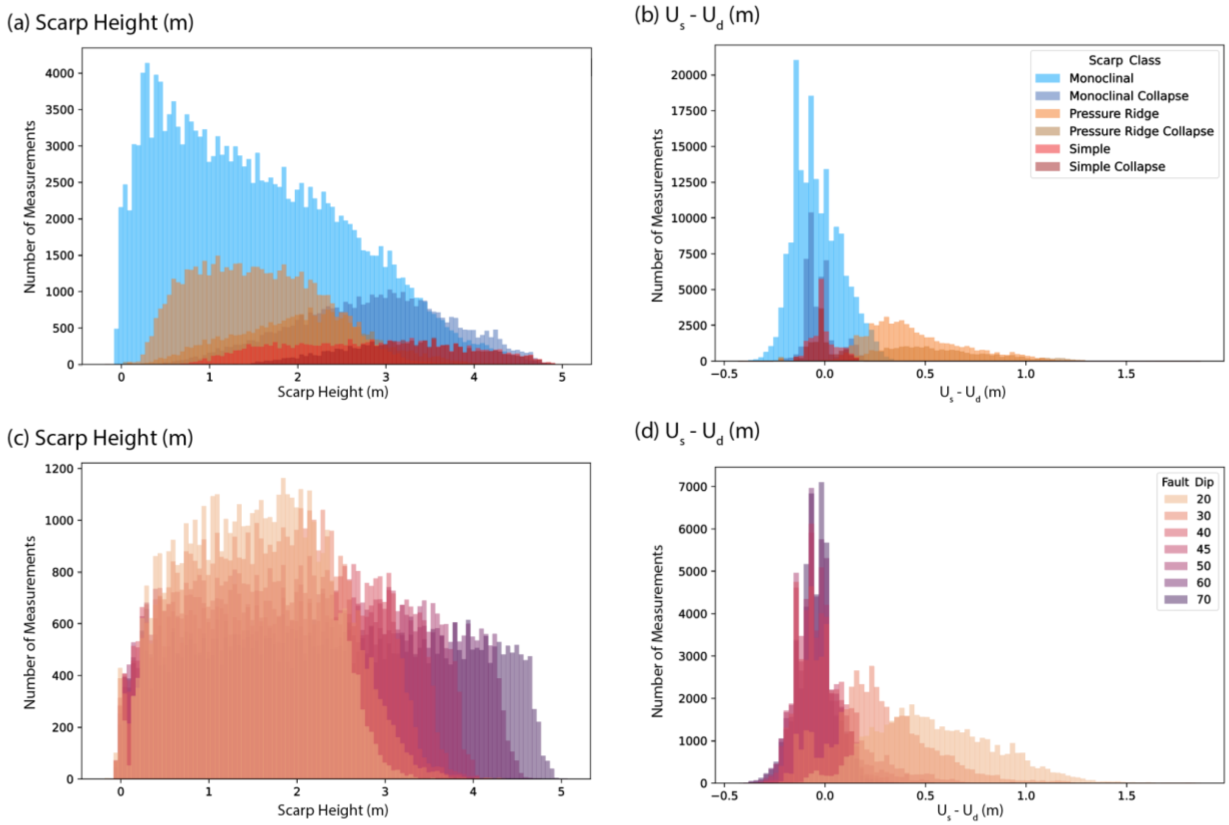

Fig. 9. Distributions of the scarp height (*left*) and the U_s - U_d (*right*) organized by (a & b) scarp class and (c & d) fault dip.

Deformation Zone Width

The deformation zone width (DZW) measurements are related to a number of the DEM model parameters. Figure 10 depicts the distribution of the DZW measurements in the dataset organized by the scarp class, sediment density, sediment depth, unruptured sediment depth above the fault tip (related to the fault seed), the sediment strength, and the fault dip. The DEM model parameters that feature the most influence on the resultant scarp morphology include the sediment depth, sediment strength, and fault dip (Fig. 10 c,e,f).

The different scarp classes each feature unique ranges of DZW (Fig. 10 a). The simple scarps have the smallest mean DZW (2.87 ± 1.68 m) as they tend to form on steep faults that primarily accommodate vertical displacement. In contrast, the pressure ridge scarps have the widest range of DZW (14.75 ± 8.04 m) because they form backthrusts that widen the deformation zone and contribute to additional uplift, secondary fractures, and splays. The monoclinal scarps are the most frequent in the dataset and have moderate deformation zone widths (6.99 ± 4.87 m) in comparison to the simple and pressure ridge scarps. The monoclinal scarps feature a triangular wedge of shear that forms through fault-propagation folding. The DZW of these scarps increases with displacement.

The DZW increases directly with the total sediment thickness above the surface of the bedrock (Fig. 10c). Thinner sediment (i.e., 3 m) yields a smaller mean DZW (4.83 ± 2.94 m) than thicker sediment profiles (i.e., 10 m; 12.79 ± 7.83 m). This is expected because the fault has less material to propagate through to reach the surface. There is a near linear relationship with the depth of sediment and the resultant deformation zone width present in the full dataset. Additionally, the unruptured sediment depth above the tip of the fault shows an influence on the DZW. Generally, more unruptured sediment above the fault tip yields a wider DZW as the fault propagates up to the surface (Fig. 10d), although this relationship is not consistent for all unruptured sediment depths.

Regarding sediment strength, the DZW decreases with increasing sediment strength (Fig. 10e). Weak sediment has the widest mean DZW (11.03 ± 7.36 m), moderate sediment has a smaller DZW (8.27 ± 6.15 m), and strong sediment has the smallest DZW (6.81 ± 5.75 m). Strong sediment localizes deformation to distinct shear planes while weaker sediment tends to yield a distributed zone of shear in the model and thus results in wider DZW (Fig 10e). We note that heterogeneous sediment strength can also influence DZW. In particular, cohesive top layers tend to localize surface deformation, thereby reducing DZW relative to similar models without this cohesive unit.

Finally, the prescribed fault dip at depth has a major influence on the DZW. Shallow faults (i.e., 20º and 30º) often develop backthrusts which significantly widen the DZW through folding and uplift (15.36 ± 8.91 m). As noted, these backthrusts form since the prescribed fault dip is shallower than the friction angle of the sediment (~32.6º) and therefore the fault must steepen as it propagates upwards, creating an axial surface at the fault bend which can concentrate slip on this plane of weakness. In contrast, steep faults (50º - 70º) localize deformation directly above the fault leading to a smaller DZW (i.e., 70º; 5.83 ± 4.37 m).

Therefore, the sediment depth, sediment strength, and fault dip contribute to the resultant DZW and patterns in the fault scarp morphology.

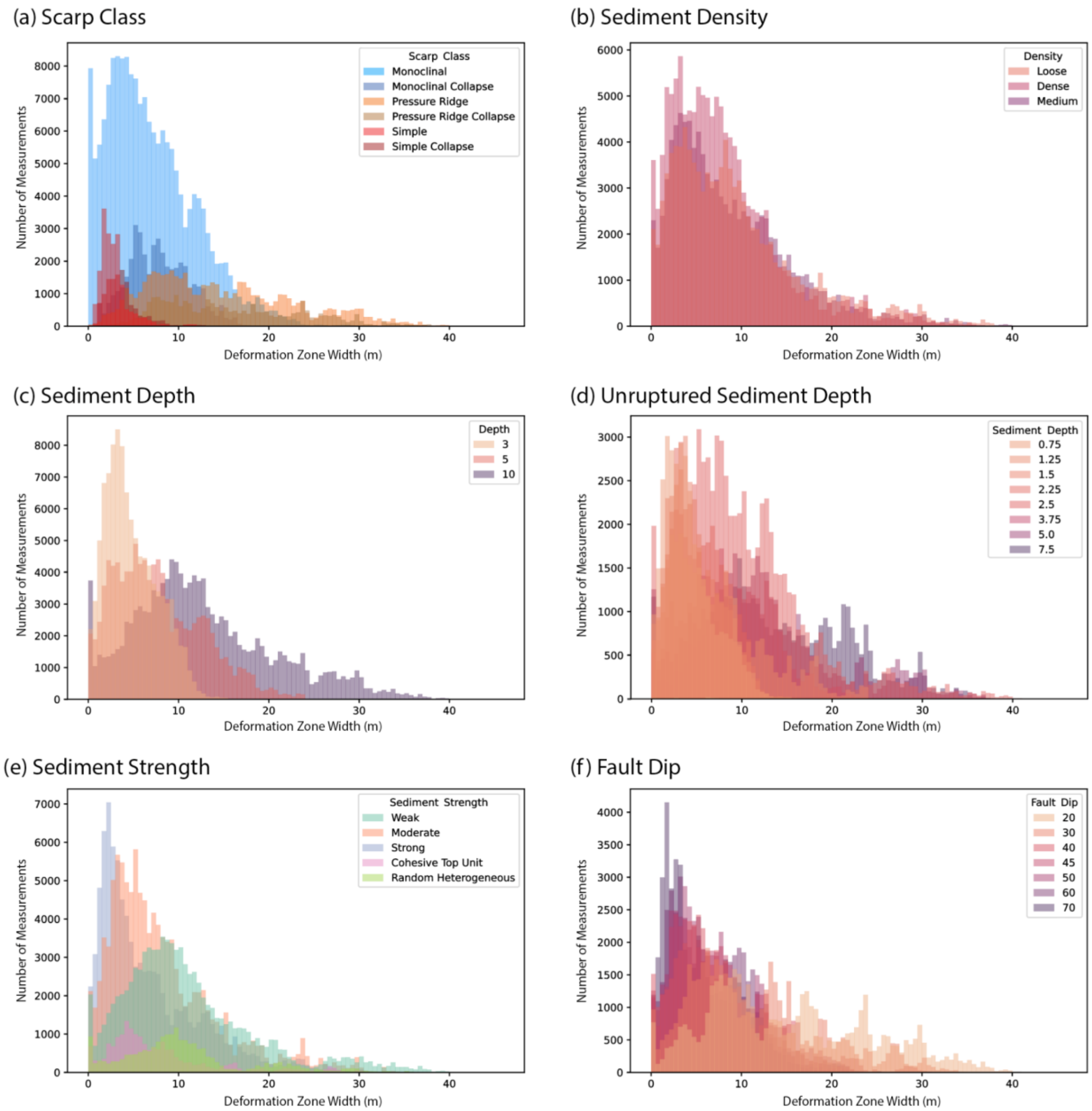

Fig. 10. Distributions of deformation zone width organized by DEM model parameters: (a) scarp classification, (b) sediment density, (c) sediment depth, (d) unruptured sediment depth (fault seed), (e) sediment strength, and (f) fault dip.

Scarp Dip

Figure 11 shows the distribution of scarp dips present in the dataset organized by scarp class, sediment density, sediment depth, unruptured sediment depth (fault seed depth), sediment strength, and fault dip.

The scarp dips in the dataset are highly dependent on the scarp type (Fig. 11a). The monoclinal (15.73º ± 9.43º), monoclinal collapse (20.77º ± 9.44º), pressure ridge (16.28º ± 9.26º), and pressure ridge collapse (17.22º ± 8.86º) scarps all present positive values of median scarp dips, often at or near the angle of repose of the sediment. Meanwhile, simple (64.12º ± 13.86º) and simple collapse scarps (77.41º ± 12.22º) are characterized by negative values of scarp dip, indicating the direct fault displacement that causes a fault scarp overhang. There are comparatively fewer simple scarps in the dataset than monoclinal or pressure ridge scarps (Fig. 11a).

The sediment strength, overall depth (Fig. 11c), and the unruptured sediment depth (Fig. 11d) influence the scarp dip. Weak sediment distributes shear throughout the sediment profile and maintains a lower angle of repose. In contrast, the strong sediment localizes slip to individual fractures and fault splays at the surface, hence why it tends to have higher overall scarp dip values. Thus, the sediment strength plays a moderate role in the localization of slip at the surface and the steepness of the scarp dip. The deepest sediment models (10 m) have the shallowest median scarp dips (12.60º ± 10.94º), moderate depth (5 m) has steeper scarp dips (19.50º ± 16.30º), and the shallowest sediment (3 m) has the steepest scarp dips (23.45º ± 20.95º). Figure 11c shows that the scarp dip increases with lower sediment depths. This is because the deeper sediment models need to accommodate more slip to reach the same scarp dip values as shallow sediment given how the fault propagates to the surface - the shear is distributed throughout the vertical sediment profile. Therefore, the sediment depth significantly contributes to how well the fault localizes slip at the surface.

Finally, the fault dip influences the scarp dip (Fig. 11f). Given the distribution shown in Figure 11f, faults steeper than the friction angle (~32.6º) of the sediment tend to form simple scarps with negative scarp dips while shallower faults (20º & 30º) rarely present scarp overhangs and instead maintain the angle of repose. The development of a negative scarp dip depends on the amount of vertical displacement of the hanging wall and the strength of the sediment to prevent hanging wall collapse. Therefore, steeper faults are more prone to forming scarp overhangs while moderate or shallow fault dips will form scarps near the angle of repose. Thus, the fault dip plays a moderate role in the steepness of the scarp dip.

In summary, the sediment depth, unruptured sediment above the fault tip, sediment strength, and fault dip contribute to the resultant scarp dip.

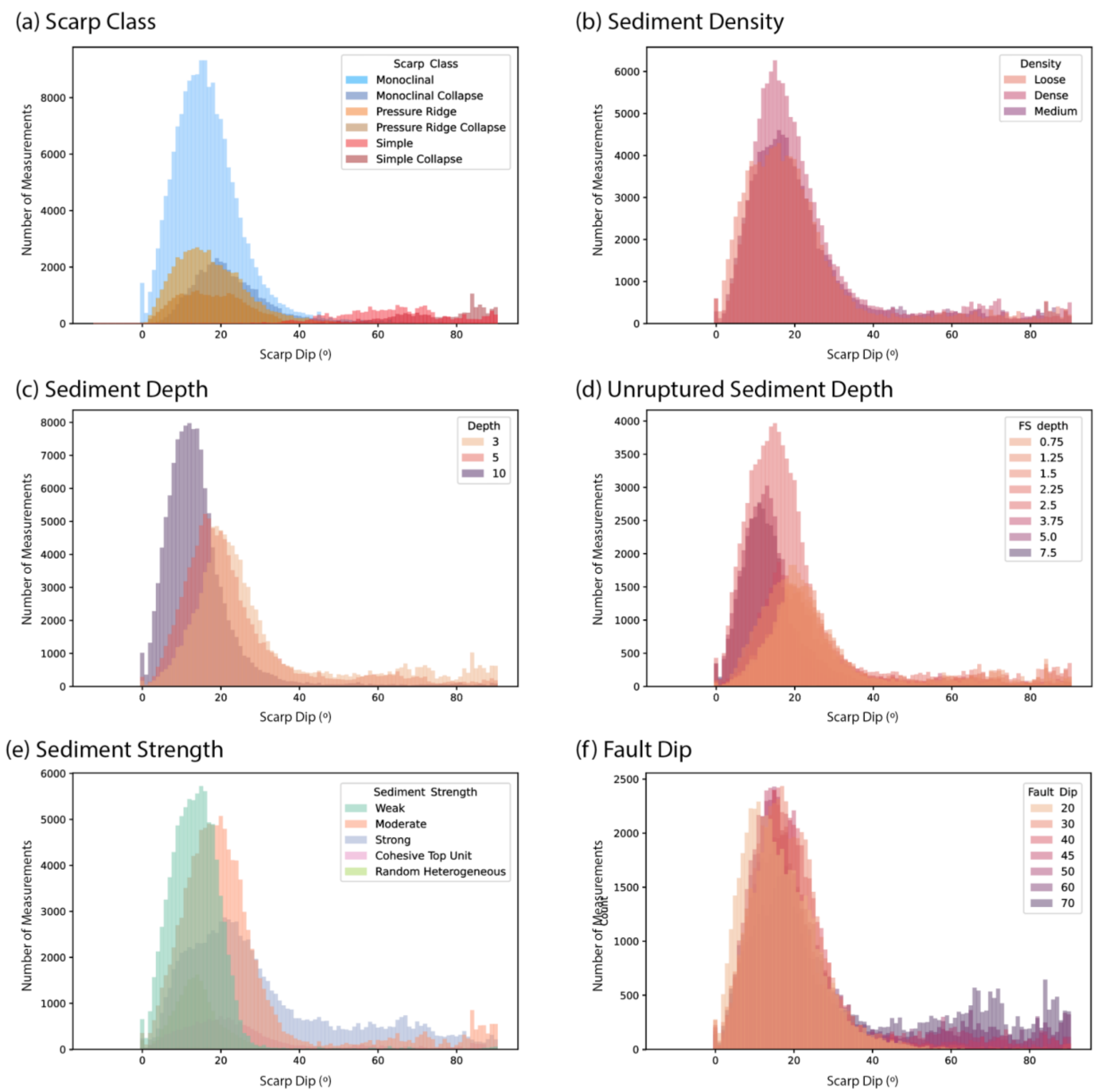

Fig. 11. Distributions of scarp dip organized by DEM model parameters: (a) scarp classification, (b) sediment density, (c) sediment depth, (d) unruptured sediment depth (fault seed), (e) sediment strength, and (f) fault dip.

COMPARISON OF DEM MODEL DATA TO NATURAL EXAMPLES

Here, we compare the DEM model ground surface deformation measurements to historic measurements of thrust and reverse fault ruptures. Our goal is to assess how well the DEM dataset captures the scale of observed surface ruptures. We do this comparison first relative to the full FDHI dataset (Sarmiento et al., 2021), then to the 1952 M 7.36 Kern County, California, earthquake.

Fault Displacement Hazard Initiative (FDHI) Dataset

The FDHI dataset (Sarmiento et al., 2021) is the most comprehensive record of surface fault rupture characteristics for historic earthquakes. The database contains measurements of ground surface ruptures for 25 thrust or reverse fault events including the scarp height, deformation zone width, as well as the principal and distributed deformation. We organized the FDHI dataset to evaluate only principal ground surface ruptures measurements of reverse or reverse-oblique events that are marked as high to moderate quality with a fault zone width < 50 m. The 50 m limit to deformation zone width reflects the maximum of our DEM model bounds and seeks to exclude distributed deformation in natural events that may have occurred across multiple, widely spaced fault strands. We plotted the results of the FDHI dataset for the principal deformation zone width and scarp height in Figure 12 colored by the earthquake name. The distribution of DEM model measurements is underlaid in grey.

There are only three events in the FDHI dataset which report the principal fault zone width (FZW, which we describe as DZW): 2005 M 7.6 Kashmir, 1952 M 7.36 Kern County, and 2008 M 7.9 Wenchuan earthquakes. Since there are not enough measurements to evaluate the probability of the principal DZW, these measurements are represented as single value (bars) over the probability of DEM model measurements of DZW in grey (Fig. 12a). Overall, the DEM model dataset distribution captures the range of FDHI measurements of DZW well (Fig. 12a).

Regarding the distribution of measured scarp heights, the FDHI dataset has three events (2013 M 7.1 Bohol, 2008 M 7.9 Wenchuan, and 1993 M 6.2 Killari earthquakes) with multiple observations across each rupture trace. These events are plotted by the count of scarp height measurements with the DEM dataset plotted by probability in Fig. 12b. Again, we note that the DEM dataset largely captures the range of measured scarp heights except for a few outliers of extreme scarp heights from the Wenchuan rupture. We suggest that these may result from the fact that the Wenchuan event was a M 7.9, while our models only extended to M 7.8, from uncertainty in field measurements, or natural variability in the earthquake rupture not captured by our models. However, the DEM dataset captures the broad range of possible natural scarp heights well, and thus we suggest provides a compliment to the very limited number of thrust and reverse fault earthquakes where ground ruptures have been measured.

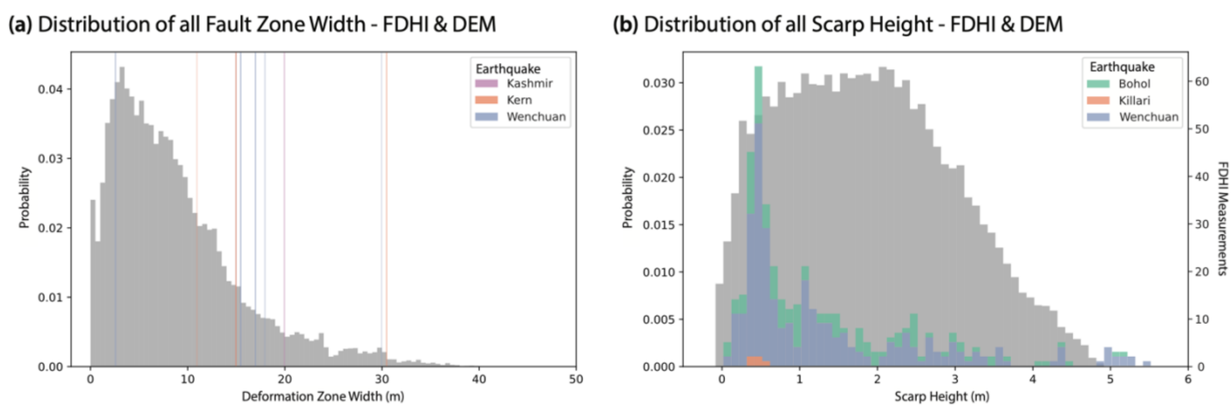

Fig. 12. Distribution of FDHI Dataset (colored by earthquake) compared to the DEM dataset (grey) of homogeneous and heterogeneous sediment ground surface deformation measurements of principal (a) deformation zone width and (b) scarp height. In a, the full DEM dataset is represented by probabilities while the FDHI values are shown as vertical bars. In b, the full DEM dataset probabilities are shown with the left axis, while the FDHI values are shown as a count of scarp height measurements with the right axis.

Case Study: 1952 M 7.36 Kern County earthquake

We perform a case study on the 1952 M 7.36 Kern County, California, earthquake focused on deformation zone width (DZW) from the FDHI dataset compared to the DEM dataset (Figure 13). The purpose of this exercise is to illustrate how the DEM dataset can be used with increasing specificity for relevant fault and model parameters to describe individual, natural earthquakes.

The FDHI dataset describes the 1952 Kern County rupture with a principal DZW of 11, 15, and 30.5 m on a 30º dipping fault. Further, they describe the rupture as a pressure ridge scarp (Sarmiento et al., 2021). We can compare the DZW measurements of Kern County to the entire distribution of the DEM dataset in Figure 13a. The broad distribution of DZW measurements in the DEM dataset captures the DZW measurements of Kern County. We then extract from the DEM dataset only the measurements that correspond with the Kern County earthquake magnitude (M 7.36 ± 0.1) and plot the DZW measurements colored by fault dip (Fig. 13b). We then show the measurements from the DEM dataset for the reported 30°fault dip (Fig. 13c) and pressure ridge scarp classification (Fig. 13d). This shows that by selecting results from the DEM model suite that best represent the Kern County event provide improved fits with the observed scarp characteristics. For example, when considering all fault dips from the DEM dataset, we note that the highest probabilities occur at lower magnitudes of DZW than observed in the Kern County rupture (Fig. 13b). The highest probabilities of DEM model measurements at low values of DZW are associated with fault dips (≥ 50°) – greater than reported for Kern County (30°) at these sites. By including DEM model results only with the appropriate fault dip (30º), we see that the distribution of measurements more closely matches the observed scarp DZW's (Fig. 13c). Moreover, at a magnitude of 7.36 on a fault dipping 30º, the DEM dataset is dominated by monoclinal and pressure ridge scarps (Fig. 13c). Notably, only the pressure ridge scarp measurements fit the entire distribution of Kern County FZW measurements. This is consistent with the observation that the scarps in the Kern County event were classified as pressure ridges by FDHI. Therefore, in Figure 13d, we show the DEM dataset organized by magnitude 7.36 ± 0.1 on a fault dipping 30º for only pressure ridge scarps. This model distribution fits the Kern County FZW measurements well.

This analysis illustrates how the DEM dataset can be used to forecast potential ground surface ruptures in future earthquakes. Specifically, we suggest that by defining event magnitude as part of an earthquake rupture forecast and relating this to an estimate of anticipated fault displacement at the surface, one can use the DEM dataset to explore the possible range of ground rupture characteristics. Such an assessment could be refined by local geologic data, including estimated values and/or ranges of the fault dip, depth of the fault tip, and sediment strength. The consistency between the DEM model results and observations from natural earthquakes suggest that such use of the model dataset would be robust. Ultimately, these model data can be seen as a way to extend the very limited number of measurements of surface scarps from thrust and reverse fault earthquakes to inform forecasts of future rupture behaviors.

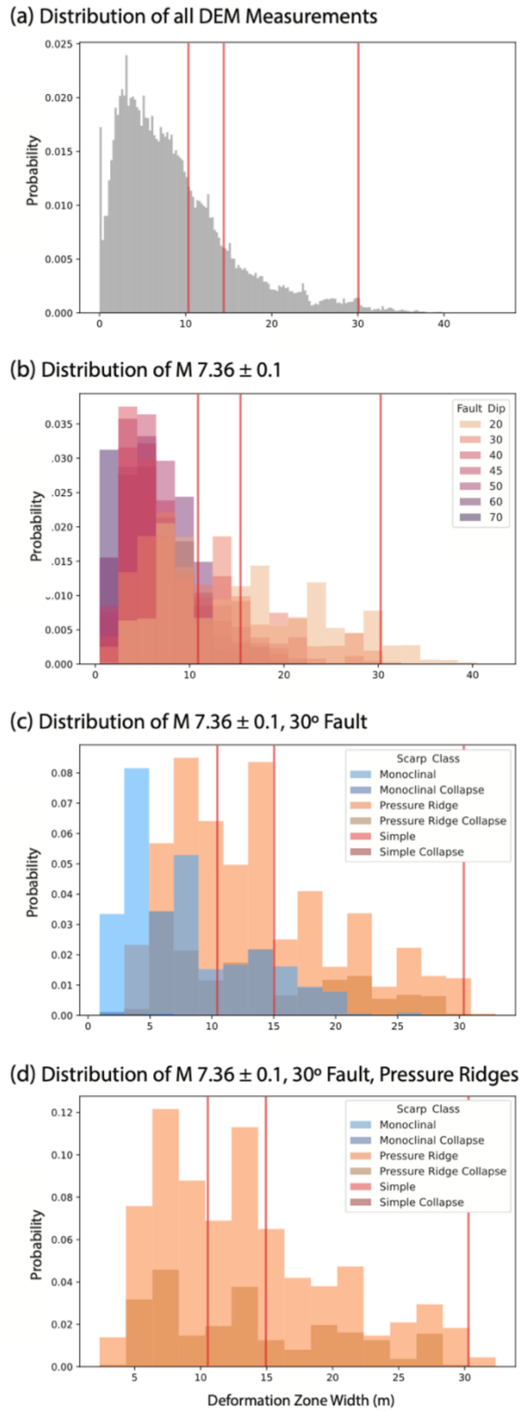

Fig. 13. (a) Distribution of all DZW measurements for homogeneous and heterogeneous DEM models plotted as a probability. Kern County principal deformation zone width measurements are represented by red lines (11, 15, and 30.5 m obtained from the FDHI dataset). (b) Distribution of DEM model measurements for a M 7.36 earthquake colored by fault dip. (c) Distribution of a M 7.36 earthquake on a 30º dipping fault colored by resultant scarp class. (d) Distribution of a M 7.36 earthquake on a 30º dipping fault for only pressure ridge and pressure ridge collapse scarps represented in the DEM dataset.

CONCLUSIONS

We employed geomechanical models to explore the influence of earthquake source characteristics and geological site parameters on fault scarp morphologies for thrust and reverse fault earthquakes. We performed a total of 3,434 DEM experiments considering the sediment depth, density, homogeneous and heterogeneous sediment strengths, fault dip, and the amount of unruptured sediment above the fault tip. We used a computer vision (CV) model to obtain measurements of ground surface deformation characteristics (scarp height, U_s - U_d, DZW, and scarp dip) for a total of 346,834 DEM model measurements taken every 0.05 m of slip. The DEM model suite describes a broad range of scarp behaviors, including monoclinal, pressure ridge, and simple scarps that can be modified by surface collapse (Chiama et al., 2023). Each scarp class has unique geomorphic features:

1. Monoclinal scarps form a single dipping panel near the angle of repose with scarp heights and deformation zone widths controlled by the accumulation of slip at depth.
2. Pressure ridge scarps form backthrusts with positive values of U_s - U_d due to additional uplift above the undeformed surface of the hanging wall which leads to the widest deformation zone widths.
3. Simple scarps form direct fault displacements with steep scarp dip angles and the smallest deformation zone widths while scarp height is controlled by the accumulation of slip at depth.

We found that the most influential parameters on the patterns of ground surface deformation are fault displacement (i.e., anticipated earthquake magnitude), fault dip, sediment depth, and sediment strength.

- The accumulation of slip and fault dip largely controls the scarp height.
- Low angle fault dips tend to develop backthrusts which contribute to positive values of U_s - U_d and wide values of DZW – as observed in pressure ridge scarps.
- Steep fault dips and strong cohesive sediment yields direct fault scarp displacements with high scarp heights, small deformation zone widths, and steep scarp dips – as observed in simple scarps.
- Weak sediment results in broad zones of distributed shear with shallow scarp dips and wide deformation zones.
- Strong sediment localizes shear bands and tends to result in rougher ground surface deformation yielding steeper scarp dips and smaller deformation zones.
- Heterogeneity in sediment strengths tends to average strength contrasts between layers, however, a cohesive top unit yields more roughness and variability of surface deformation characteristics.

Finally, we compared the DEM model results to surface rupture measurements in the FDHI database. This analysis showed that the model results effectively describe the range of surface rupture observations, with improved fits obtained by incorporating additional information about the earthquake size, fault geometry, and surface deformation style. This suggest that the DEM results can be used to augment field datasets and help to forecast patterns of ground surface deformation in future earthquakes given specific anticipated source and site characteristics.

ACKNOWLEDGEMENTS

This work was supported using Itasca, Particle Flow Code 2D (PFC2D) version 7.00. The authors would specifically like to thank the Itasca support and developers for their guidance in developing the model structure and code. This research was supported by the National Science Foundation (NSF), Division of Earth Sciences (EAR), Tectonics Program, Grant Number 2207119; and by the Southern California Earthquake Center (SCEC) Agreement Number 110862181 (SCEC Award Number 22013), which is funded by the prime award National Science Foundation Award Number EAR-1600087. The authors would like to thank Lydia Bailey, Emily Carrero-Mustelier, Benjamin Chauvin, Jessica Don, Estefan F. Garcia, Michael Naylor Hudgins, Brendan Meade, Brook Runyon, Lluis Salo-Salgado, Natasha Toghramadjian, and Robert Welch for thoughtful discussions and coding suggestions. The authors thank the reviewers for their comments and suggestions that greatly improved the article.

DECLARATION OF CONFLICTING INTERESTS

The author(s) declared no potential conflicts of interest with respect to the research, authorship, and/or publication of this article.

FUNDING STATEMENT

This research was supported by the National Science Foundation (NSF), Division of Earth Sciences (EAR), Tectonics Program, Grant Number 2207119; and by the Southern California Earthquake Center (SCEC) Agreement Number 110862181 (SCEC Award Number 22013), which is funded by the prime award National Science Foundation Award Number EAR-1600087.

DATA AND RESOURCES

The 2D DEM model code used for these experiments and the code framework for a general biaxial stress test are available at https://github.com/kchiama?tab=repositories (last accessed June 2024) for reproducibility. The CV model code is available at: https://github.com/willbed34/ScarpClassificationPaper (last accessed June 2024). A dataset containing the DEM model parameters and measured ground surface deformation characteristics (presented in Fig. 5 – 13), the DEM code, PFC2D SAV files, CSV files of the particle locations every 0.5 m of slip for every experiment, and animations of every DEM experiment are available on DesignSafe (Chiama et al., 2024b,c). The data for DEM models and ground surface deformation measurements presented in this paper are available open-access on DesignSafe (doi: https://doi.org/10.17603/ds2-xpq0-gw80, doi: https://doi.org/10.17603/ds2-gfsj-pp60).

REFERENCES

Allmendinger, R.W., 1998, Inverse and forward numerical modeling of trishear fault-propagation folds: Tectonics, v. 17, p. 640–656.

Baize, S. et al., 2019, A worldwide and unified database of surface ruptures (SURE) for fault displacement hazard analyses: Seismological Research Letters, v. 91, p. 499–520, doi:10.1785/0220190144.

Benesh, N.P., Plesch, A., Shaw, J.H., and Frost, E.K., 2007, Investigation of growth fault bend folding using discrete element modeling: Implications for signatures of active folding above blind thrust faults: Journal of Geophysical Research: Solid Earth, v. 112, p. 1–10, doi:10.1029/2006JB004466.

Benesh, N.P., and Shaw, J.H., 2023, A mechanical basis of fault-bend folding: AAPG Bulletin, v. 107, p. 1529–1552, doi:10.1306/04192321198.

Biasi, G.P., and Weldon, R.J., 2006, Estimating Surface Rupture Length and Magnitude of Paleoearthquakes from Point Measurements of Rupture Displacement: Bulletin of the Seismological Society of America, v. 96, p. 1612–1623, doi:10.1785/0120040172.

Boncio, P., Liberi, F., Caldarella, M., and Nurminen, F.C., 2018, Width of surface rupture zone for thrust earthquakes: Implications for earthquake fault zoning: Natural Hazards and Earth System Sciences, v. 18, p. 241–256, doi:10.5194/nhess-18-241-2018.

Bransby, M.F., Davies, M.C.R., El Nahas, A., and Nagaoka, S., 2008, Centrifuge modelling of reverse fault-foundation interaction: Bulletin of Earthquake Engineering, v. 6, p. 607–628, doi:10.1007/s10518-008-9080-7.

Chen, W.S. et al., 2001, 1999 Chi-Chi earthquake: A case study on the role of thrust-ramp structures for generating earthquakes: Bulletin of the Seismological Society of America, v. 91, p. 986–994, doi:10.1785/0120000731.

Chen, R., and Petersen, M.D., 2019, Improved implementation of rupture location uncertainty in fault displacement hazard assessment: Bulletin of the Seismological Society of America, v. 109, p. 2132–2137, doi:10.1785/0120180305.

Chiama, K., Chauvin, B., Plesch, A., Moss, R., and Shaw, J.H., 2023, Geomechanical Modeling of Ground Surface Deformation Associated with Thrust and Reverse-Fault Earthquakes: A Distinct Element Approach: Bulletin of the Seismological Society of America, v. 113, p. 1702–1723, doi:10.1785/0120220264.

Chiama, K., Bednarz, W., Moss, R., Shaw, J. H., (2024a) Identification and analysis of ground surface rupture patterns from thrust and reverse fault earthquakes using geomechanical models, Japanese Geotechnical Society Special Publication, 10(26), 978-983, https://doi.org/10.3208/jgssp.v10.OS-15-06.

Chiama, K., W. Bednarz, R. Moss, A. Plesch, J. Shaw. (2024b) "Homogeneous 2D DEM Experiments", in Influence of sediment depth, sediment strength, fault dip, and slip on fault scarp morphology in thrust and reverse fault earthquakes using 2D Distinct Element Method (DEM) models. DesignSafe-CI. https://doi.org/10.17603/ds2-xpq0-gw80

Chiama, K., W. Bednarz, R. Moss, A. Plesch, J. Shaw. (2024c) "Heterogeneous 2D DEM Experiments", in Influence of sediment depth, sediment strength, fault dip, and slip on fault scarp morphology in thrust and reverse fault earthquakes using 2D Distinct Element Method (DEM) models. DesignSafe-CI. https://doi.org/10.17603/ds2-gfsj-pp60

Clark, A. (2015). Pillow (PIL Fork) Documentation. Retrieved from https://buildmedia.readthedocs.org/media/pdf/pillow/latest/pillow.pdf, last accessed: July 1, 2024.

Cole, D.A., and Lade, P.V., 1984, Influence zones in alluvium over dip-slip faults: Journal of Geotechnical Engineering, v. 110, p. 599–615, doi:10.1061/(ASCE)0733-9410(1984)110:5(599).

Cundall, P.A., and Strack, O.D.L., 1979, A discrete numerical model for granular assemblies: Geotechnique, v. 29, p. 47–65.

Egholm, D.L., Clausen, O.R., Sandiford, M., Kristensen, M.B., and Korstgård, J.A., 2008, The mechanics of clay smearing along faults: Geology, v. 36, p. 787, doi:10.1130/G24975A.1.

Egholm, D.L., Sandiford, M., Clausen, O.R., and Nielsen, S.B., 2007, A new strategy for discrete element numerical models: 2. Sandbox applications: Journal of Geophysical Research: Solid Earth, v. 112, p. 1–12, doi:10.1029/2006JB004558.

Erickson, S.G., Strayer, L.M., and Suppe, J., 2001, Initiation and reactivation of faults during movement over a thrust-fault ramp: Numerical mechanical models: Journal of Structural Geology, v. 23, p. 11–23, doi:10.1016/S0191-8141(00)00074-2.

Erickson, S.G., Strayer, L.M., and Suppe, J., 2004, Numerical Modeling of Hinge-zone Migration in Fault-bend Folds: , p. 438–452.

Erslev, E.A., 1991, Trishear fault-propagation folding: Geology, p. 617–620.

Faccioli, E., Anastasopoulos, I., Gazetas, G., Callerio, A., and Paolucci, R., 2008, Fault rupture–foundation interaction: selected case histories: Bulletin of Earthquake Engineering, v. 6, p. 557–583, doi:10.1007/s10518-008-9089-y.

Finch, E., Hardy, S., and Gawthorpe, R., 2003, Discrete element modelling of contractional fault- propagation folding above rigid basement fault blocks: Journal of Structural Geology, v. 25, p. 515–528, doi:10.1016/S0191-8141(02)00053-6.

Finch, E., Hardy, S., and Gawthorpe, R., 2004, Discrete-element modelling of extensional fault-propagation folding above rigid basement fault blocks: Basin Research, v. 16, p. 489–506, doi:10.1111/j.1365-2117.2004.00241.x.

Fu, B., Shi, P., Guo, H., Okuyama, S., Ninomiya, Y., and Wright, S., 2011, Surface deformation related to the 2008 Wenchuan earthquake, and mountain building of the Longmen Shan, eastern Tibetan Plateau: Journal of Asian Earth Sciences, v. 40, p. 805–824, doi:10.1016/j.jseaes.2010.11.011.

Garcia, F.E., and Bray, J.D., 2018a, Distinct element simulations of earthquake fault rupture through materials of varying density: Soils and Foundations, v. 58, p. 986–1000, doi:10.1016/j.sandf.2018.05.009.

Garcia, F.E., and Bray, J.D., 2018b, Distinct Element Simulations of Shear Rupture in Dilatant Granular Media: International Journal of Geomechanics, v. 18, p. 04018111, doi:10.1061/(asce)gm.1943-5622.0001238.

Guo, Y., and Morgan, J.K., 2004, Influence of normal stress and grain shape on granular friction: Results of discrete element simulations: Journal of Geophysical Research: Solid Earth, v. 109, p. 1–16, doi:10.1029/2004JB003044.

Hardy, S., and Cardozo, N., 2021, Discrete Element Modelling of Sedimentation and Tectonics: Implications for the Growth of Thrust Faults and Thrust Wedges in Space and Time, and the Interpretation of Syn-Tectonic (Growth) Strata: Frontiers in Earth Science, v. 9, p. 742204, doi:10.3389/feart.2021.742204.

Hardy, S., and Finch, E., 2006, Discrete element modelling of the influence of cover strength on basement-involved fault-propagation folding: Tectonophysics, v. 415, p. 225–238, doi:10.1016/j.tecto.2006.01.002.

Hardy, S., and Finch, E., 2005, Discrete-element modelling of detachment folding: Basin Research, v. 17, p. 507–520, doi:10.1111/j.1365-2117.2005.00280.x.

Hardy, S., and Finch, E., 2007, Mechanical stratigraphy and the transition from trishear to kink-band fault-propagation fold forms above blind basement thrust faults: A discrete-element study: Marine and Petroleum Geology, v. 24, p. 75–90, doi:10.1016/j.marpetgeo.2006.09.001.

Harris, C.R., Millman, K.J., van der Walt, S.J. et al. (2020) Array programming with NumPy. Nature 585, 357–362, doi:10.1038/s41586-020-2649-2.

Hubbard, J., and Shaw, J.H., 2009, Uplift of the Longmen Shan and Tibetan plateau, and the 2008 Wenchuan (M = 7.9) earthquake: Nature, v. 458, p. 194–197, doi:10.1038/nature07837.

Hughes, A.N., 2020, Mechanical controls on structural styles in shortening environments: A discrete-element modelling approach: Geological Society Special Publication, v. 490, p. 33–55, doi:10.1144/SP490-2019-114.

Hughes, A.N., Benesh, N.P., and Shaw, J.H., 2014, Factors that control the development of fault-bend versus fault-propagation folds: Insights from mechanical models based on the discrete element method (DEM): Journal of Structural Geology, v. 68, p. 121–141, doi:10.1016/j.jsg.2014.09.009.

Hughes, A.N., and Shaw, J.H., 2014, Fault displacement-distance relationships as indicators of contractional fault-related folding style: AAPG Bulletin, v. 98, p. 227–251, doi:10.1306/05311312006.

Hughes, A.N., and Shaw, J.H., 2015, Insights into the mechanics of fault-propagation folding styles: Bulletin of the Geological Society of America, v. 127, p. 1752–1765, doi:10.1130/B31215.1.

Hunter, J.D. (2007) Matplotlib: A 2D Graphics Environment, Computing in Science & Engineering, vol. 9(3), 90-95.

Imber, J., Tuckwell, G.W., Childs, C., Walsh, J.J., Manzocchi, T., Heath, A.E., Bonson, C.G., and Strand, J., 2004, Three-dimensional distinct element modelling of relay growth and breaching along normal faults: Journal of Structural Geology, v. 26, p. 1897–1911, doi:10.1016/j.jsg.2004.02.010.

Itasca, 1999, PFC2D: Theory and Background, User's Guide, Command Reference, FISH in PFC2D: Minneapolis, MN, USA, Itasca Consulting Group.

Kelson, K.I., Kang, K.H., Page, W.D., Lee, C.T., and Cluff, L.S., 2001, Representative styles of deformation along the Chelungpu Fault from the 1999 Chi-Chi (Taiwan) earthquake: Geomorphic characteristics and responses of man-made structures: Bulletin of the Seismological Society of America, v. 91, p. 930–952, doi:10.1785/0120000741.

Lee, J.C., Chen, Y.G., Sieh, K., Mueller, K., Chen, W.S., Chu, H.T., Chan, Y.C., Rubin, C., and Yeats, R., 2001, A vertical exposure of the 1999 surface rupture of the Chelungpu Fault at Wufeng, Western Taiwan: Structural and Paleoseismic implications for an active thrust fault: Bulletin of the Seismological Society of America, v. 91, p. 914–929, doi:10.1785/0120000742.

Li, Y., Jia, D., Shaw, J.H., Hubbard, J., Lin, A., Wang, M., Luo, L., Li, H., and Wu, L., 2010, Structural interpretation of the coseismic faults of the Wenchuan earthquake: Three-dimensional modeling of the Longmen Shan fold-and-thrust belt: Journal of Geophysical Research: Solid Earth, v. 115, doi:10.1029/2009JB006824.

Litchfield, N.J. et al., 2018, Surface rupture of multiple crustal faults in the 2016 Mw 7.8 Kaikōura, New Zealand, earthquake: Bulletin of the Seismological Society of America, v. 108, p. 1496–1520, doi:10.1785/0120170300.

Mora, P., and Place, D., 1998, Numerical simulation of earthquake faults with gouge' toward a comprehensive explanation for the heat flow paradox: Journal of Geophysical Research, v. 103.

Mora, P., and Place, D., 1999, The weakness of earthquake faults: Geophysical Research Letters, v. 26, p. 123–126, doi:10.1029/1998GL900231.

Morgan, J.K., 2015, Effects of cohesion on the structural and mechanical evolution of fold and thrust belts and contractional wedges: Discrete element simulations: Journal of Geophysical Research: Solid Earth, v. 120, p. 3870–3896, doi:10.1002/2014JB011455.Received.

Morgan, J.K., 1999, Numerical simulations of granular shear zones using the distinct element method: 2. Effects of particle size distribution and interparticle friction on mechanical behavior: Journal of Geophysical Research: Solid Earth, v. 104, p. 2721–2732, doi:10.1029/1998jb900055.

Morgan, J.K., 2004, Particle dynamics simulations of rate- and state-dependent frictional sliding of granular fault gouge: Pure and Applied Geophysics, v. 161, p. 1877–1891, doi:10.1007/s00024-004-2537-y.

Morgan, J.K., and Boettcher, M.S., 1999, Numerical simulations of granular shear zones using the distinct element method: 1. Shear zone kinematics and the micromechanics of localization: Journal of Geophysical Research: Solid Earth, v. 104, p. 2703–2719, doi:10.1029/1998JB900056.

Morgan, J.K., and McGovern, P.J., 2005a, Discrete element simulations of gravitational volcanic deformation: 1. Deformation structures and geometries: Journal of Geophysical Research: Solid Earth, v. 110, p. 1–22, doi:10.1029/2004JB003252.

Morgan, J.K., and McGovern, P.J., 2005b, Discrete element simulations of gravitational volcanic deformation: 2. Mechanical analysis: Journal of Geophysical Research: Solid Earth, v. 110, p. 1–13, doi:10.1029/2004JB003253.

Moss, R.E.S., and Ross, Z.E., 2011, Probabilistic fault displacement hazard analysis for reverse faults: Bulletin of the Seismological Society of America, v. 101, p. 1542–1553, doi:10.1785/0120100248.

Naylor, M., Sinclair, H.D., Willett, S., and Cowie, P.A., 2005, A discrete element model for orogenesis and accretionary wedge growth: Journal of Geophysical Research: Solid Earth, v. 110, p. 1–16, doi:10.1029/2003JB002940.

Nicol, A. et al., 2018, Preliminary geometry, displacement, and kinematics of fault ruptures in the epicentral region of the 2016 Mw 7.8 Kaikōura, New Zealand, earthquake: Bulletin of the Seismological Society of America, v. 108, p. 1521–1539, doi:10.1785/0120170329.

Pedregosa, F., Varoquaux, G., Gramfort, A., Michel, V., et al. (2011) Scikit-learn: Machine Learning in Python, Journal of Machine Learning Research, 12, 2825-2830, https://www.jmlr.org/papers/volume12/pedregosa11a/pedregosa11a.pdf.

Petersen, M.D., Dawson, T.E., Chen, R., Cao, T., Wills, C.J., Schwartz, D.P., and Frankel, A.D., 2011, Fault displacement hazard for strike-slip faults: Bulletin of the Seismological Society of America, v. 101, p. 805–825, doi:10.1785/0120100035.

Philip, H., Rogozhin, E., Cisternas, A., Bousquet, J.C., Borisov, B., and Karakhanian, A., 1992, The Armenian earthquake of 1988 December 7: faulting and folding, neotectonics and palaeoseismicity: Geophysical Journal International, v. 110, p. 141–158, doi:10.1111/j.1365-246X.1992.tb00718.x.

Rimando, J.M., Aurelio, M.A., Dianala, J.D.B., Taguibao, K.J.L., Agustin, K.M.C., Berador, A.E.G., and Vasquez, A.A., 2019, Coseismic Ground Rupture of the 15 October 2013 Magnitude (MW) 7.2 Bohol Earthquake, Bohol Island, Central Philippines: Tectonics, v. 38, p. 2558–2580, doi:10.1029/2019TC005503.

Sarmiento, A. et al., 2021, Fault Displacement Hazard Initiative Database: Natural Hazards Risk & Resiliency Research Center B. John Garrick Institute for the Risk Sciences, v. Report GIR, doi:10.34948/N36P48.

Strayer, L.M., Erickson, S.G., and Suppe, J., 2004, Influence of growth strata on the evolution of fault-related folds - Distinct-element models: AAPG Memoir, v. 82, p. 413–437.

Strayer, L.M., and Hudleston, P.J., 1997, Numerical modeling of fold initiation at thrust ramps: Journal of Structural Geology, v. 19, p. 551–566, doi:10.1016/s0191-8141(96)00109-5.

Strayer, L.M., Hudleston, P.J., and Lorig, L.J., 2001, A numerical model of deformation and fluid-flow in an evolving thrust wedge: Tectonophysics, v. 335, p. 121–145, doi:10.1016/S0040-1951(01)00052-X.

Strayer, L.M., and Suppe, J., 2001, Out-of-plane motion of a thrust sheet during along-strike propagation of a thrust ramp: A distinct-element approach: Journal of Structural Geology, v. 24, p. 637–650, doi:10.1016/S0191-8141(01)00115-8.

Van Rossum, G. (2020). The Python Library Reference, release 3.8.2. Python Software Foundation.

Walt, S., Schönberger, J.L., Nunez-Iglesias, J., Boulogne, F., Warner, J.D., Yager, N., et al. (2014) Scikit-image: Image processing in Python, PeerJ 2:e453, https://doi.org/10.7717/peerj.453

Wells, D.L., and Coppersmith, K.J., 1994, New Empirical Relationships among Magnitude, Rupture Length, Rupture Width, Rupture Area, and Surface Displacement: Bulletin of the Seismological Society of America, v. 84, p. 974–1002, doi:https://doi.org/10.1785/BSSA0840040974.

Wesnousky, S.G., 2008, Displacement and geometrical characteristics of earthquake surface ruptures: Issues and implications for seismic-hazard analysis and the process of earthquake rupture: Bulletin of the Seismological Society of America, v. 98, p. 1609–1632, doi:10.1785/0120070111.

Xu, X., Wen, X., Yu, G., Chen, G., Klinger, Y., Hubbard, J., and Shaw, J., 2009, Coseismic reverse- and oblique-slip surface faulting generated by the 2008 Mw 7.9 Wenchuan earthquake, China: Geology, v. 37, p. 515–518, doi:10.1130/G25462A.1.

Youngs, R.R. et al., 2003, A methodology for probabilistic fault displacement hazard analysis (PFDHA): Earthquake Spectra, v. 19, p. 191–219, doi:10.1193/1.1542891.

Summary of Experiments

In summary, we explored the parameter space spanned by nine initial sedimentary assemblages of varying density and thickness, seven dip angles for the fault, three fault tip depths and 13 combinations of sediment cohesion and tensile strength with our 2457 homogeneous experiments. We performed an additional two experiments on the unruptured sediment above the fault tip, from no fault seed to a full fault seed that ruptures to the surface, for a total of 2459 experiments.

Out of 975 heterogeneous experiments, 756 exhaustively probed our nine initial sedimentary assemblages, all seven dip angles for the fault, three fault tip depths and four sediment strength configurations (weak, moderate and strong vertical gradients and a set for the cohesive top unit). 210 experiments explored 10 randomized strength layering cases in one sediment assemblage for all seven fault dips and three fault tip depths. Nine experiments used a sedimentary assemblage with alternating strength layering for three fault dips and three fault tip depths.

Flowchart depicting model parameters, experiments, and modeling stages:

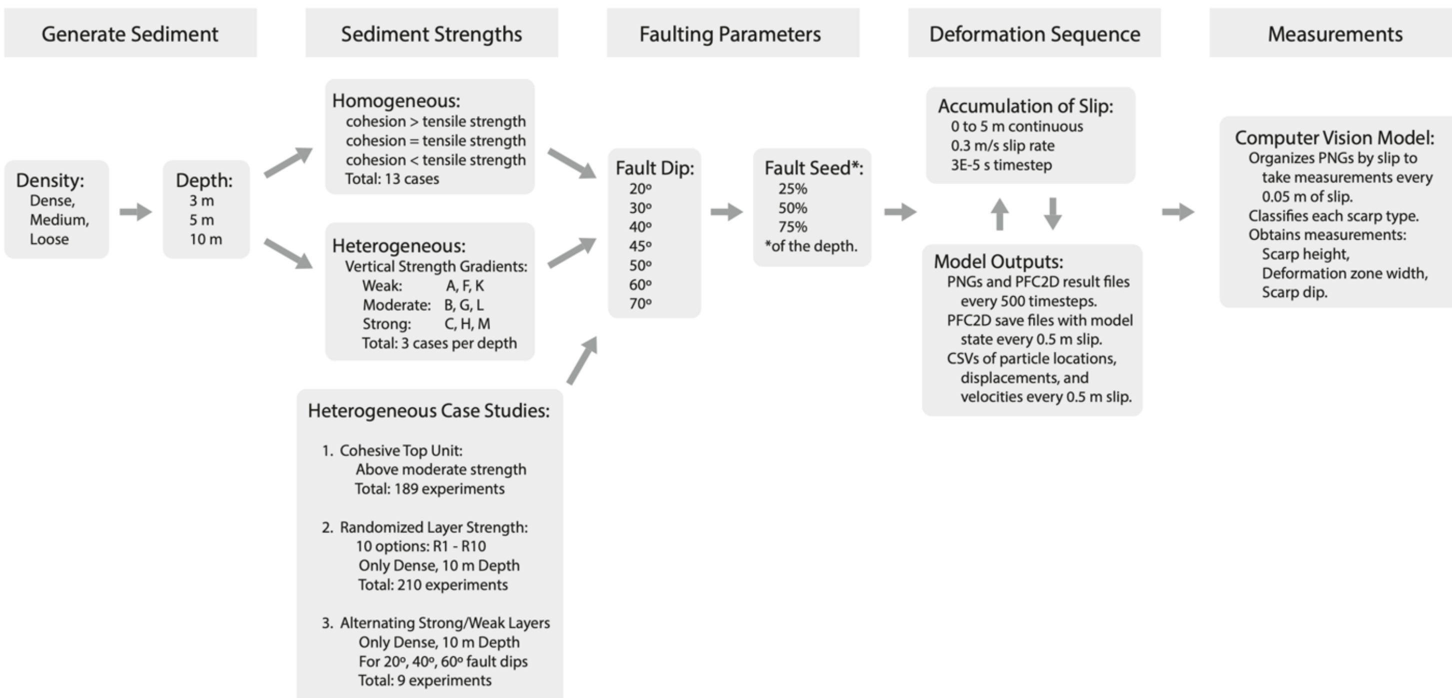

Detailed Experiment Outline:

PFC DEM Model Workflow and Trial Proposal

① Boundary Criteria:

Model Width: 50 m

Particle Size: 50x sand sized

Initial Friction Coefficient: 0.0, 0.25, 0.5
General Porosity: Dense, Medium-Dense, Loose

Total Sediment Thickness: 10, 5, and 3 m

Number of Pregrowth Layers: 0, 3, 5, and 10

Gravitational settling of particles to a stable equilibrium.
Level the topography and resettle to equilibrium.

Unbonded.sav

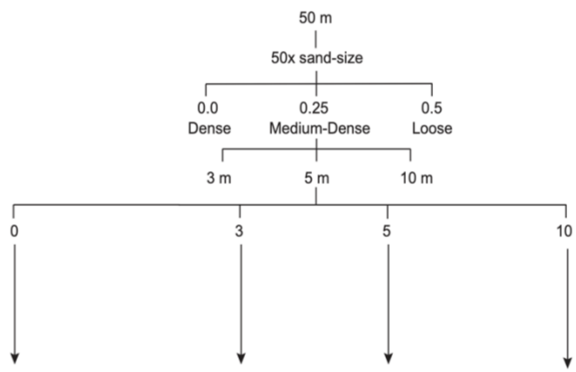

Heterogeneous Sediment (Color Key):

Strength:	Color:	HEX:
0.1		00306F
0.2		004697
0.25		002BFF
0.3		0058BC
0.4		006DDB
0.5		1D79FF
0.6		009FFA
0.7		00C2F9
0.75		71BFFF
0.8		76ECFF
0.9		E5E5E5
1.0		CCCCCC
1.1		999999
1.2		FFDC3D
1.25		FF9933
1.3		FFB000
1.4		FF8500
1.5		FF4901
1.6		EF0000
1.7		CE0000
1.75		CC0000
1.8		B7001F
1.9		990000
2.0		730013

② Sediment Mechanics:

Constant Parameters:
Parallel Bond Contact Model
Density = 2600 kg/m²
Friction Angle: 32.6°
Radius of Bonds = 0.1
Damping Ratio = 0.7
Particle Friction Coefficient = 0.3
Friction of Boundary Walls = 1.0

coh = cohesive strength of bonds
ten = tensile strength of bonds

Homogeneous (MPa)

coh ≠ ten		coh = ten		coh ≠ ten	
1.0	0.1	0.1	0.1	0.1	1.0
1.0	0.5	0.5	0.5	0.5	1.0
1.0	1.0	1.0	1.0	1.0	1.0
1.0	1.5	1.5	1.5	1.5	1.0
1.0	2.0	2.0	2.0	2.0	1.0

Heterogeneous (MPa)

A	B	C	Q
0.1	0.5	1.0	2.0
0.5	1.0	1.5	1.0
1.0	1.5	2.0	1.0

Weak → Strong

F	G	H	Q
0.1	0.5	1.0	2.0
0.25	0.75	1.25	1.0
0.5	1.0	1.5	1.0
0.75	1.25	1.75	1.0
1.0	1.5	2.0	1.0

Weak → Strong

K	L	M	Q
0.1	0.6	1.1	2.0
0.2	0.7	1.2	1.0
0.3	0.8	1.3	1.0
0.4	0.9	1.4	1.0
0.5	1.0	1.5	1.0
0.6	1.1	1.6	1.0
0.7	1.2	1.7	1.0
0.8	1.3	1.8	1.0
0.9	1.4	1.9	1.0
1.0	1.5	2.0	1.0

Weak → Strong

Random Sediment Mechanics for Heterogeneous Tests:

	R1	R2	R3	R4	R5	R6	R7	R8	R9	R10
Unit 1	0.4	1.1	0.6	1.7	0.1	1.4	1.8	0.2	1.2	0.3
Unit 2	0.7	2.0	1.1	0.5	0.4	0.3	1.2	1.0	1.5	1.3
Unit 3	1.8	1.7	1.5	1.9	1.1	0.1	1.4	1.1	1.3	1.8
Unit 4	1.7	0.8	0.2	0.8	1.9	1.0	1.0	0.6	0.3	1.2
Unit 5	1.1	1.5	1.4	2.0	0.9	0.4	1.1	1.9	0.2	0.9
Unit 6	0.3	1.8	1.2	0.9	0.8	1.2	0.8	1.6	0.8	0.8
Unit 7	1.3	0.1	1.8	1.3	1.6	0.7	0.3	0.8	1.7	0.1
Unit 8	1.5	1.2	1.9	0.1	1.8	0.5	0.6	1.3	1.4	1.4
Unit 9	1.2	1.9	0.8	0.3	2.0	0.6	1.3	1.4	0.9	1.0
Unit 10	1.9	1.3	0.9	1.0	0.6	1.7	1.9	0.4	2.0	0.7

Top Layer ↑ Bottom Layer

2,459 Homogeneous Experiments

756 Heterogeneous Experiments

Dense, 10 m deep on all fault dips & all FS: 210 experiments

The mechanical properties are set and the sediment settles to an equilibrium.

Homogeneous.sav or **Heterogeneous.sav**

279 Sediment Mechanical Configurations

③ Deformation Sequence:

Fault Dip Angle: 20°, 30°, 40°, 45°, 50°, 60° and 70°

Fault Seed Length: 25%, 50%, and 75%

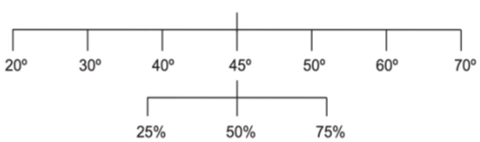

3425 Trials

Constant Parameters:
Amount of Slip: 0 - 5 m continuous
Slip Rate = 0.3 m/s
Timestep: 3E-5 s
9E-6 m of displacement in each timestep
Fault Friction Coefficient = 0.3

Driving wall drives the deformation of the particles at a timestep of 3E-5 until the maximum amount of prescribed fault slip (5 m) is reached.
Gravitational settling of particles to a stable equilibrium.

Last_deformation_stage.sav

Supplemental Figures

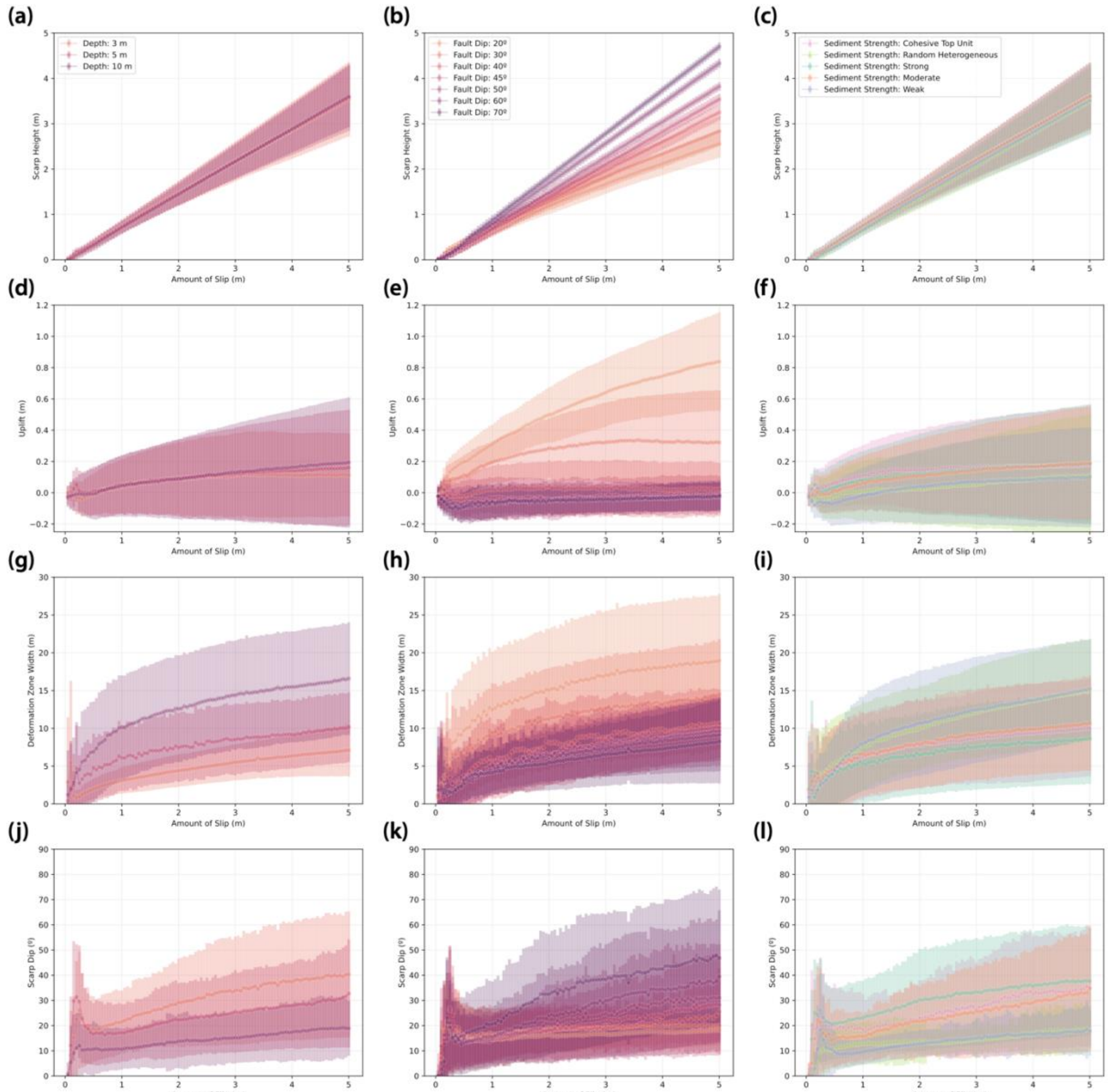

Figure S1: Influence of the (a,d,g,j) sediment depth, (b,e,h,k) fault dip, and (c,f,I,l) sediment strength on the (a,b,c) scarp height, (d,e,f) uplift, (g,h,i) DZW, and (j,k,l) scarp dip.

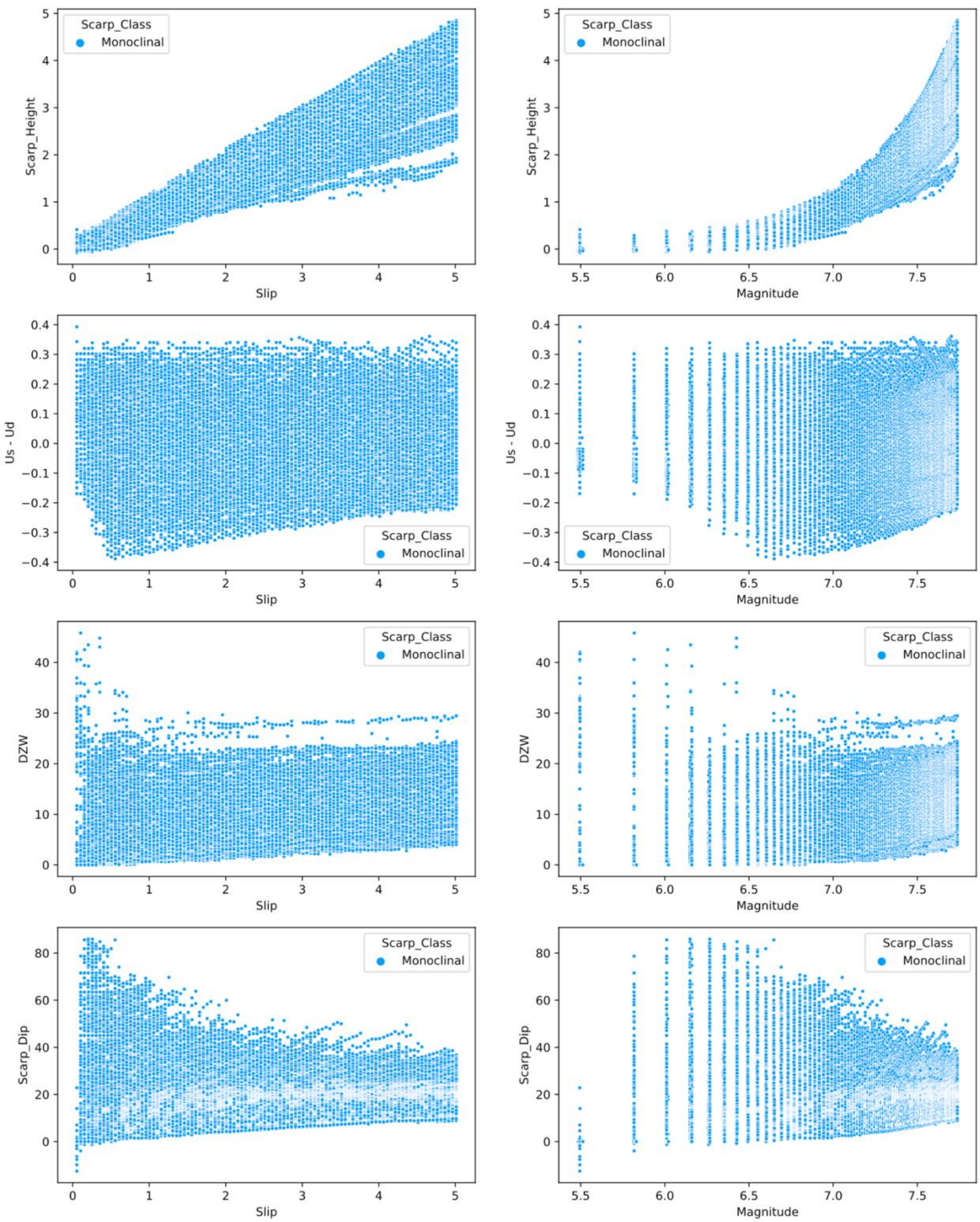

Figure S2: Monoclinal scarps plotted by the accumulation of slip (*left*) and estimated earthquake magnitude (*right*) by the scarp height, uplift, DZW, and scarp dip (*top to bottom*).

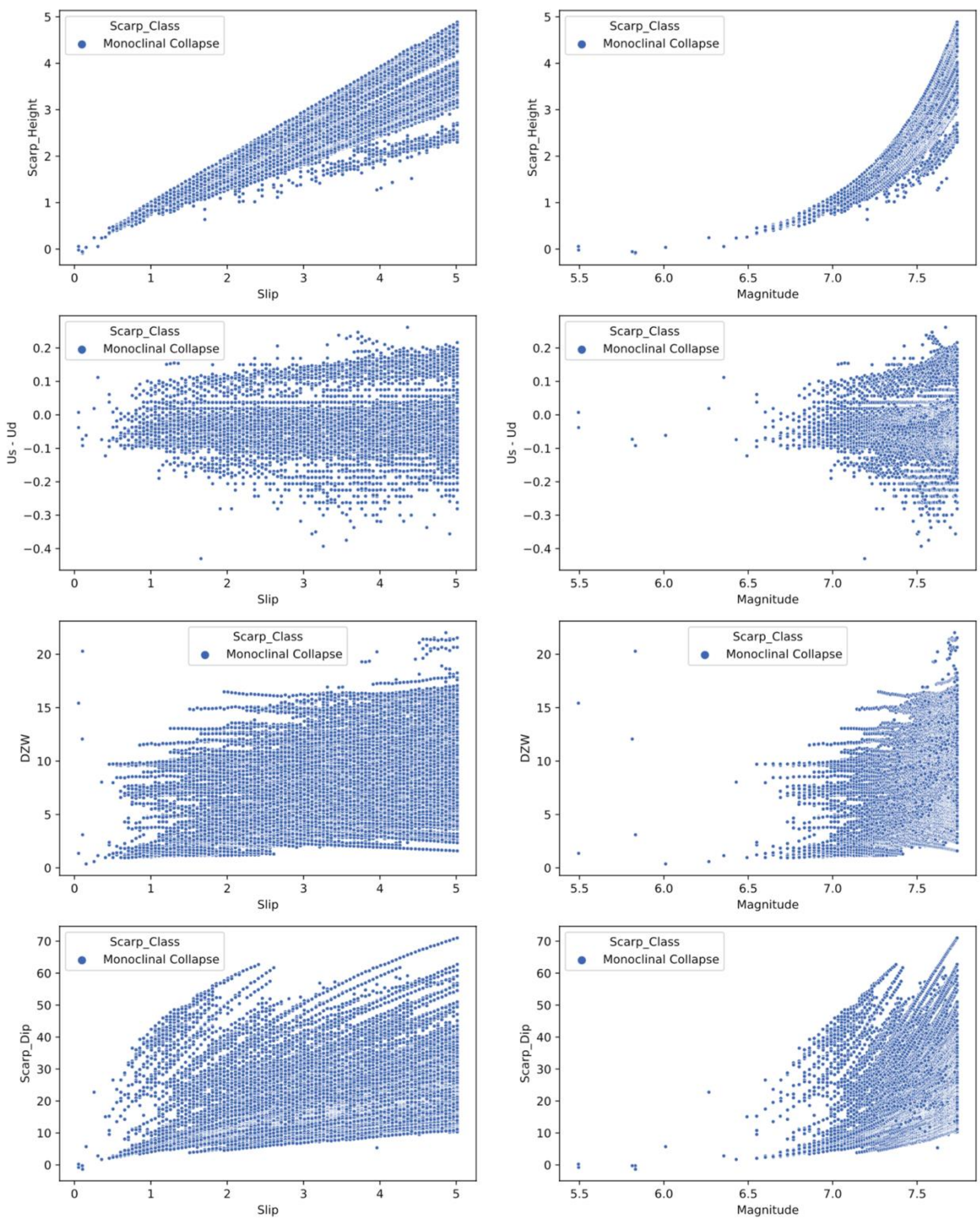

Figure S3: Monoclinal collapse scarps plotted by the accumulation of slip (*left*) and estimated earthquake magnitude (*right*) by the scarp height, uplift, DZW, and scarp dip (*top to bottom*).

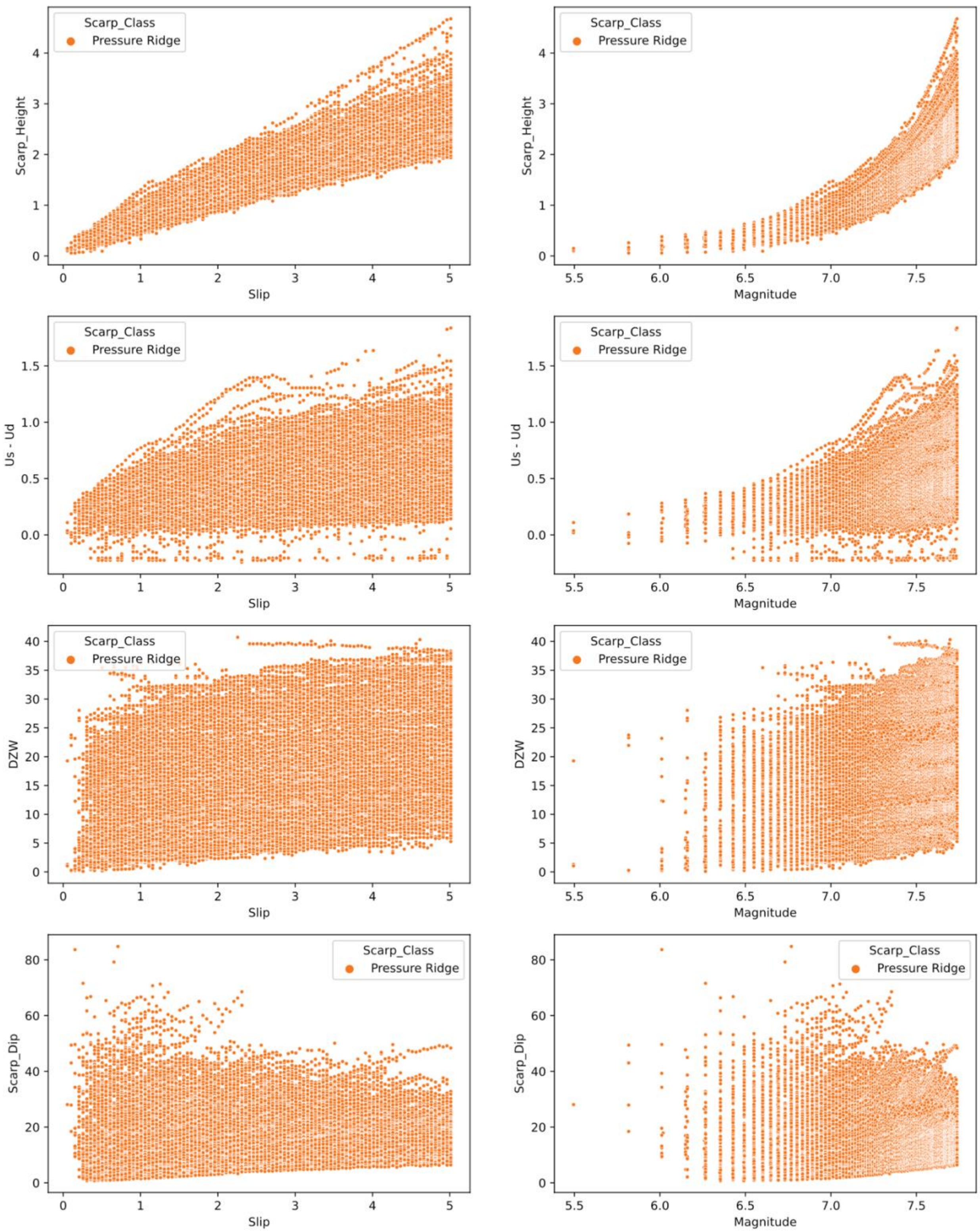

Figure S4: Pressure ridge scarps plotted by the accumulation of slip (*left*) and estimated earthquake magnitude (*right*) by the scarp height, uplift, DZW, and scarp dip (*top to bottom*).

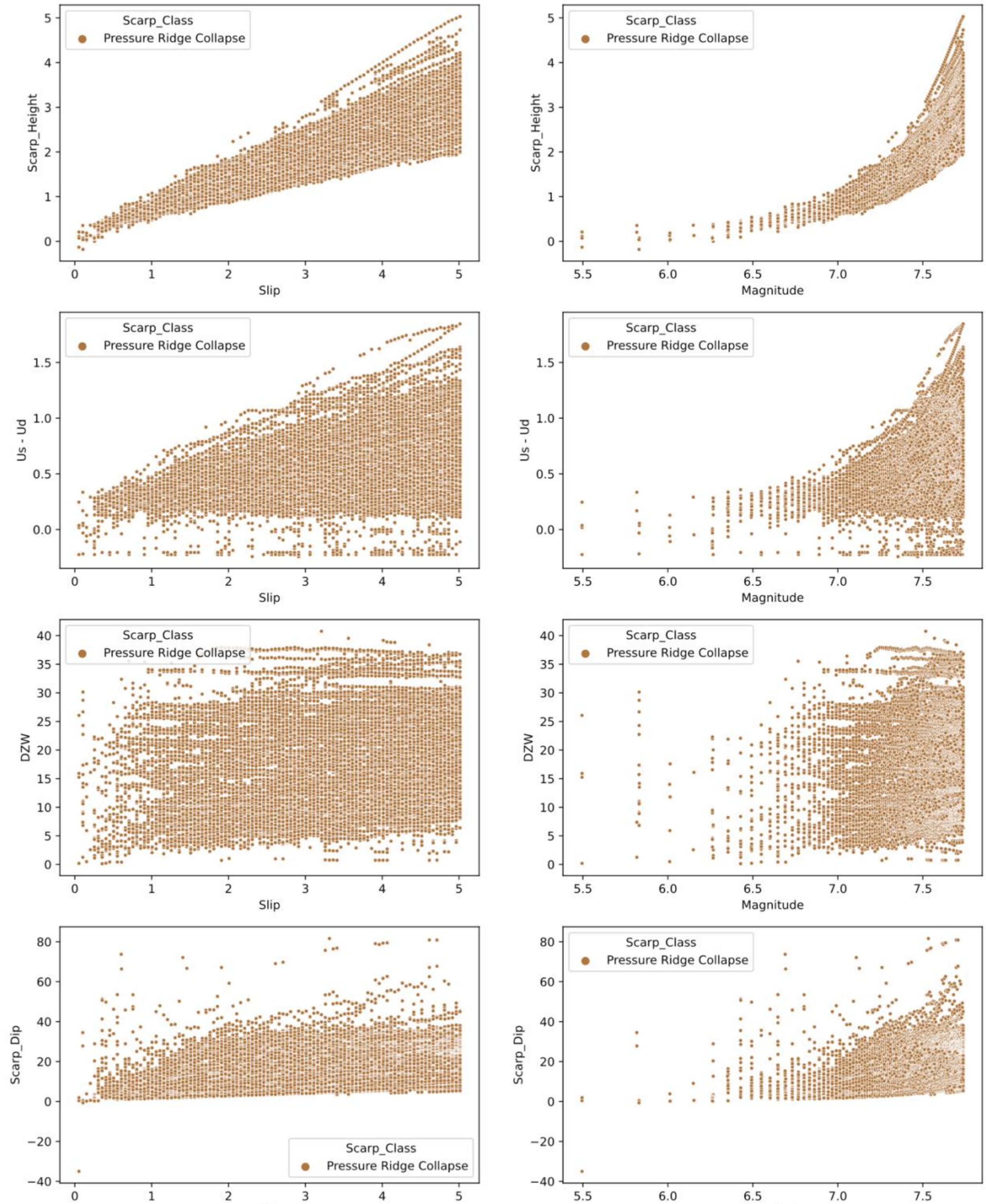

Figure S5: Pressure ridge collapse scarps plotted by the accumulation of slip (*left*) and estimated earthquake magnitude (*right*) by the scarp height, uplift, DZW, and scarp dip (*top to bottom*).

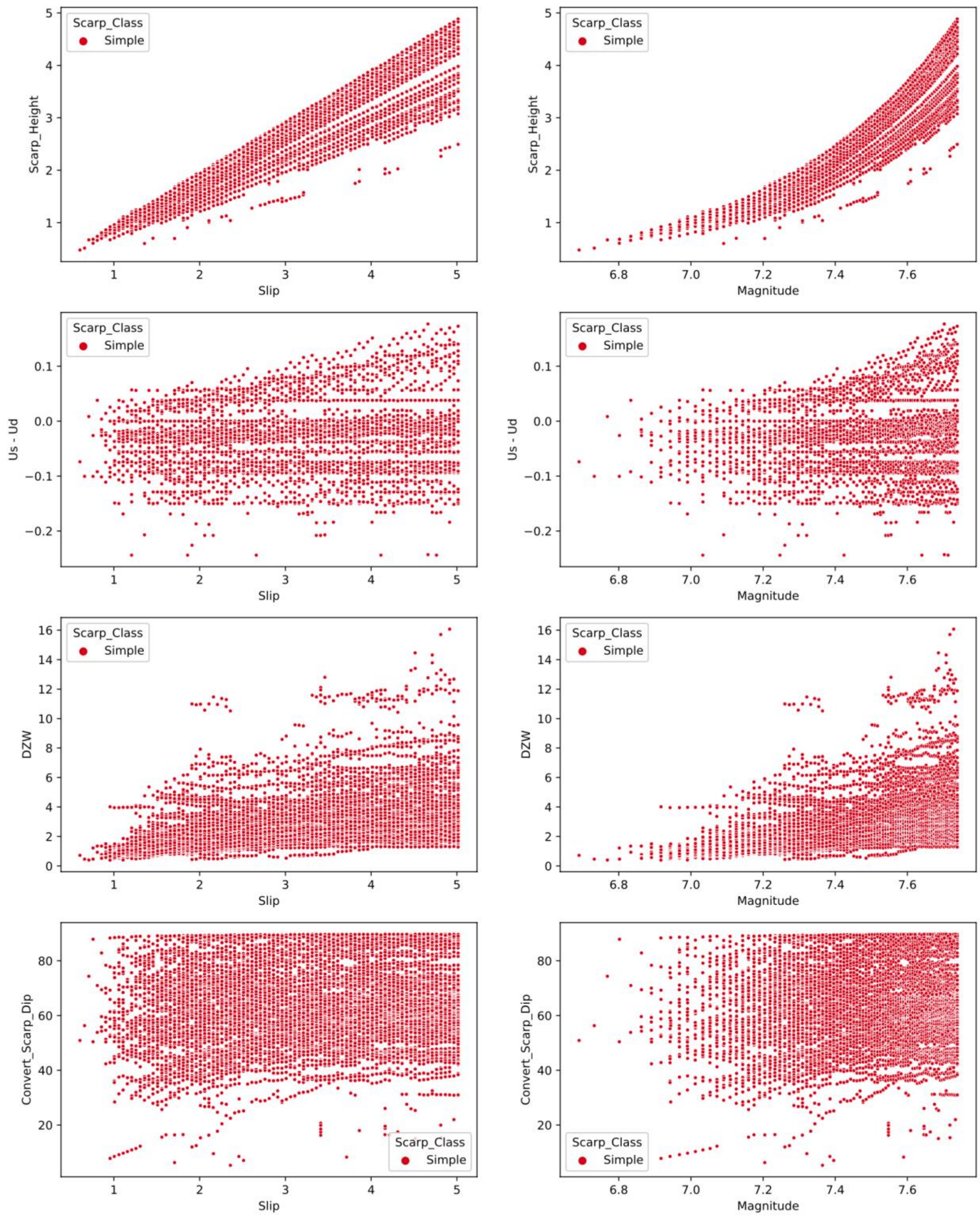

Figure S6: Simple scarps plotted by the accumulation of slip (*left*) and estimated earthquake magnitude (*right*) by the scarp height, uplift, DZW, and scarp dip (*top to bottom*).

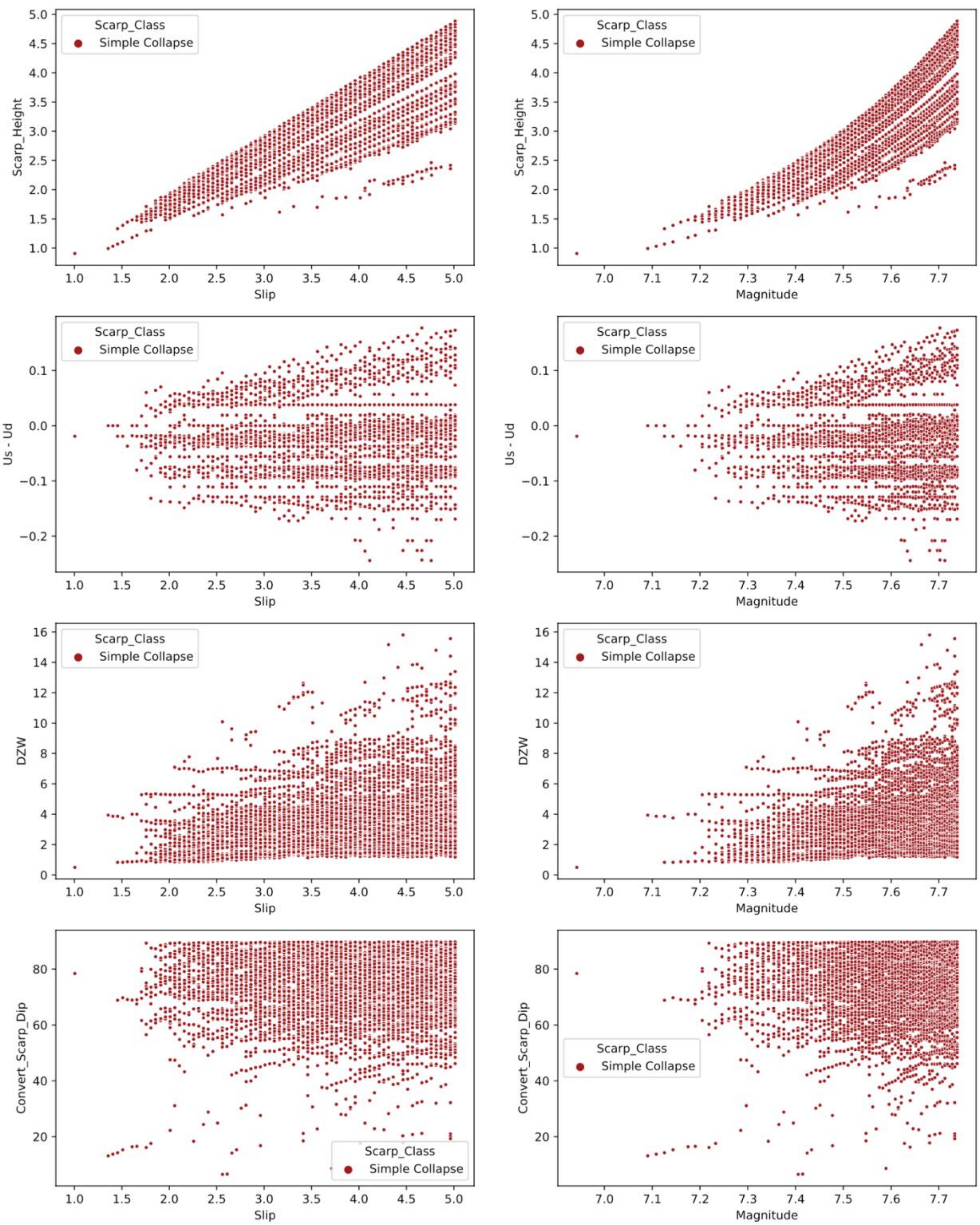

Figure S7: Simple collapse scarps plotted by the accumulation of slip (*left*) and estimated earthquake magnitude (*right*) by the scarp height, uplift, DZW, and scarp dip (*top to bottom*).

Vertical Sediment Gradients: 567 experiments.
AFK experiments: vertically weak sediment gradients

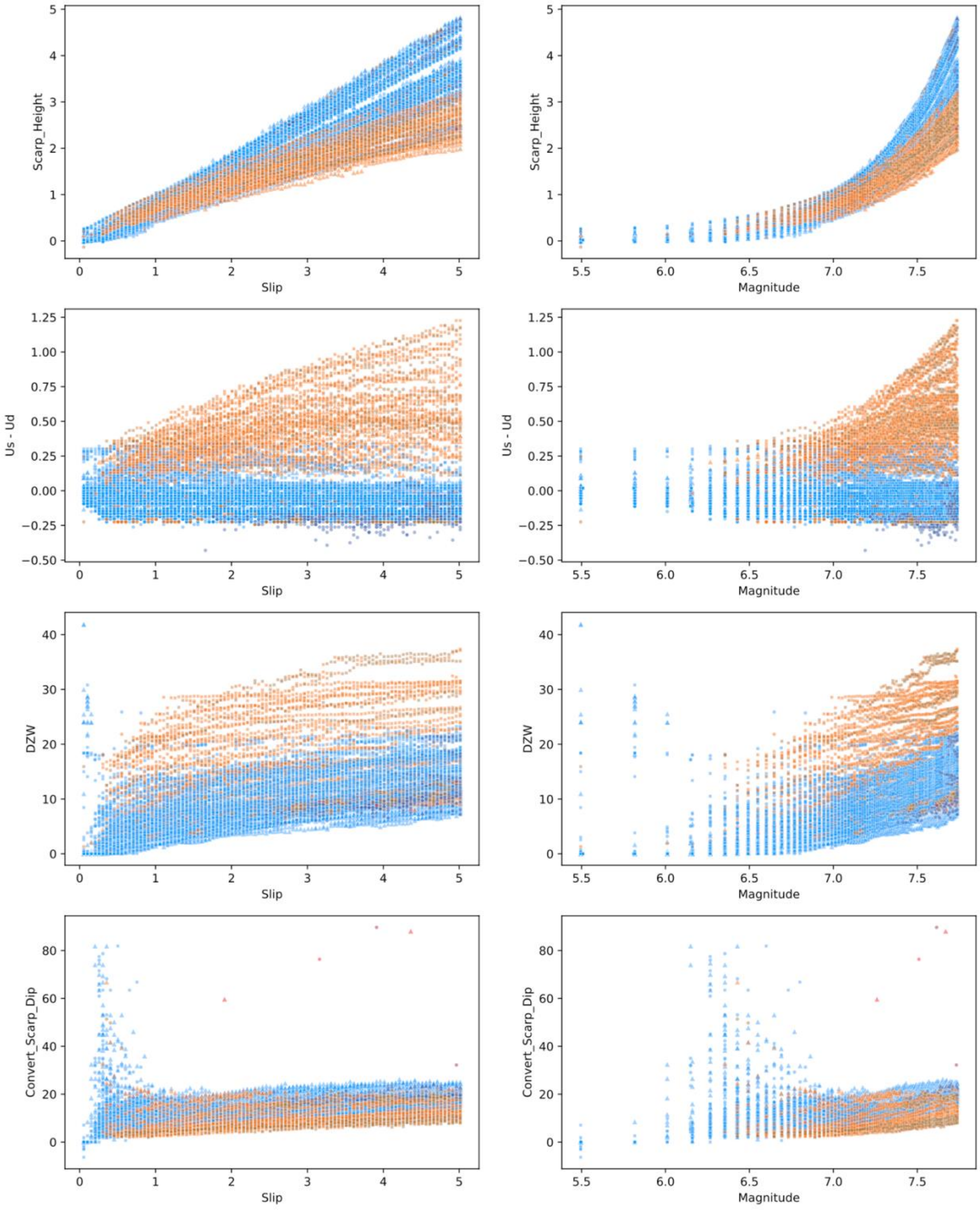

Figure S8: Heterogeneous experiments plotted by the accumulation of slip (*left*) and estimated earthquake magnitude (*right*) by the scarp height, uplift, DZW, and scarp dip (*top to bottom*).

BGL experiments: vertically moderate sediment gradients

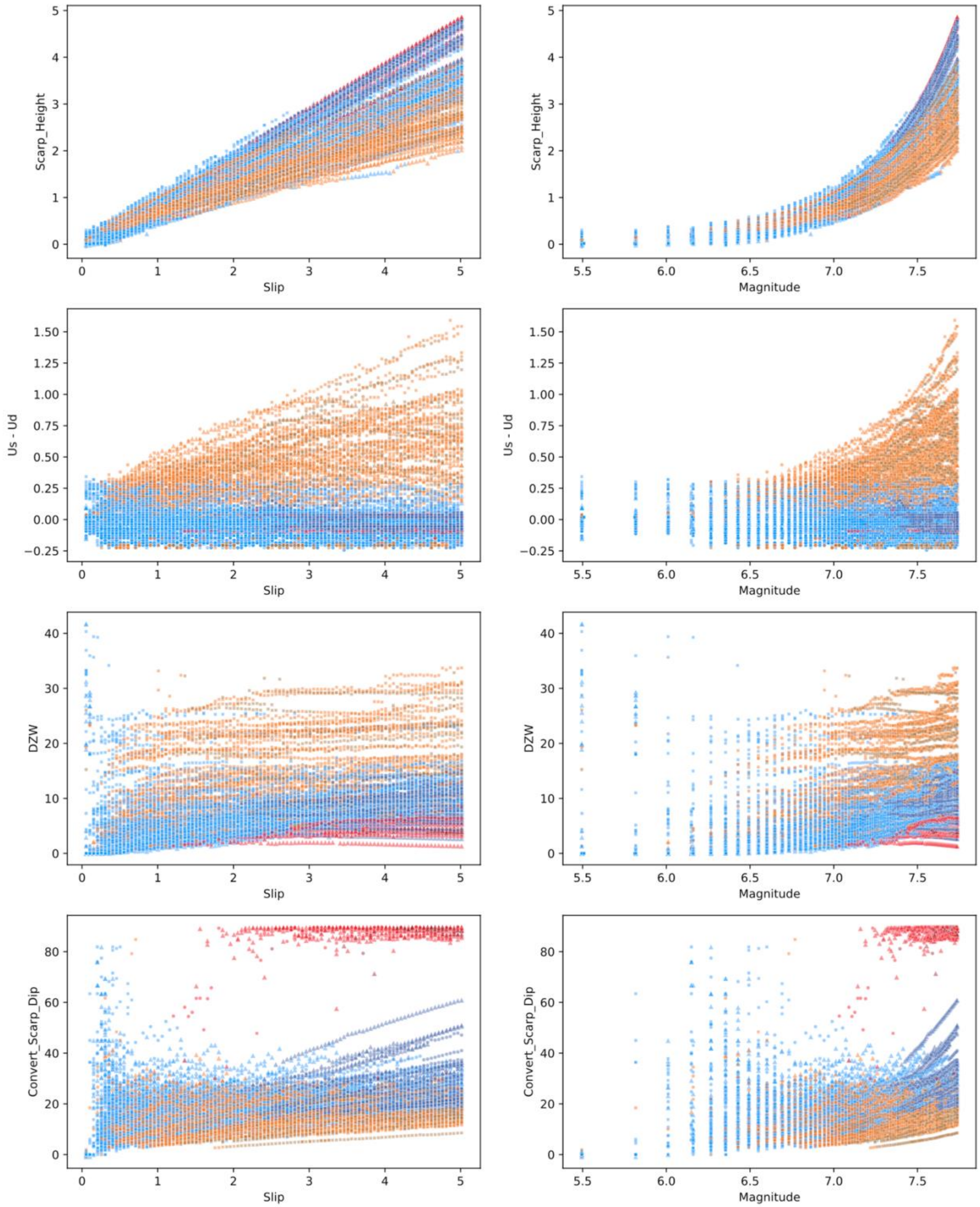

Figure S9: Heterogeneous experiments plotted by the accumulation of slip (*left*) and estimated earthquake magnitude (*right*) by the scarp height, uplift, DZW, and scarp dip (*top to bottom*).

CHM experiments: vertically strong sediment gradients

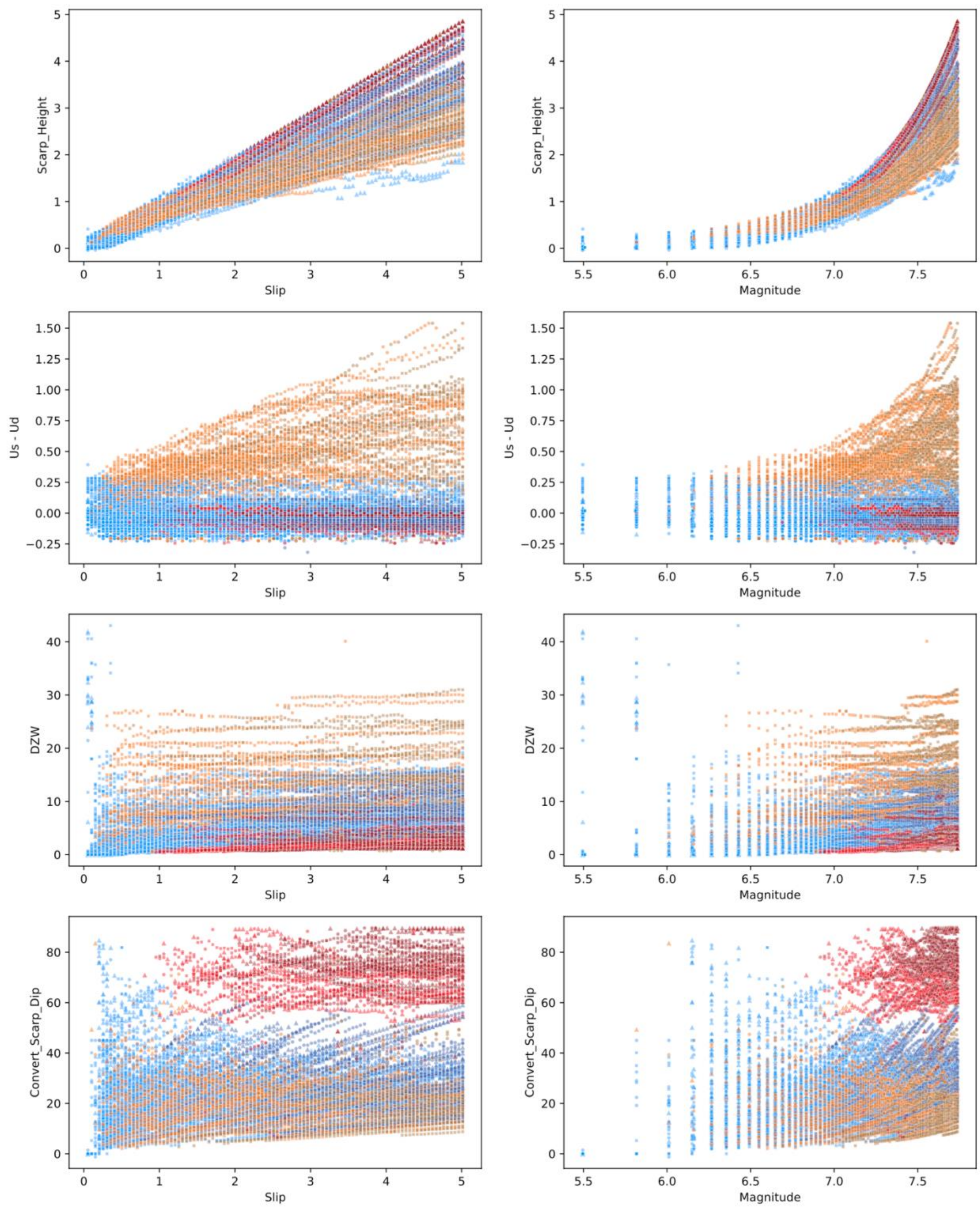

Figure S10: Heterogeneous experiments plotted by the accumulation of slip (*left*) and estimated earthquake magnitude (*right*) by the scarp height, uplift, DZW, and scarp dip (*top to bottom*).

Vertically Randomized Sediment Strengths: 210 experiments

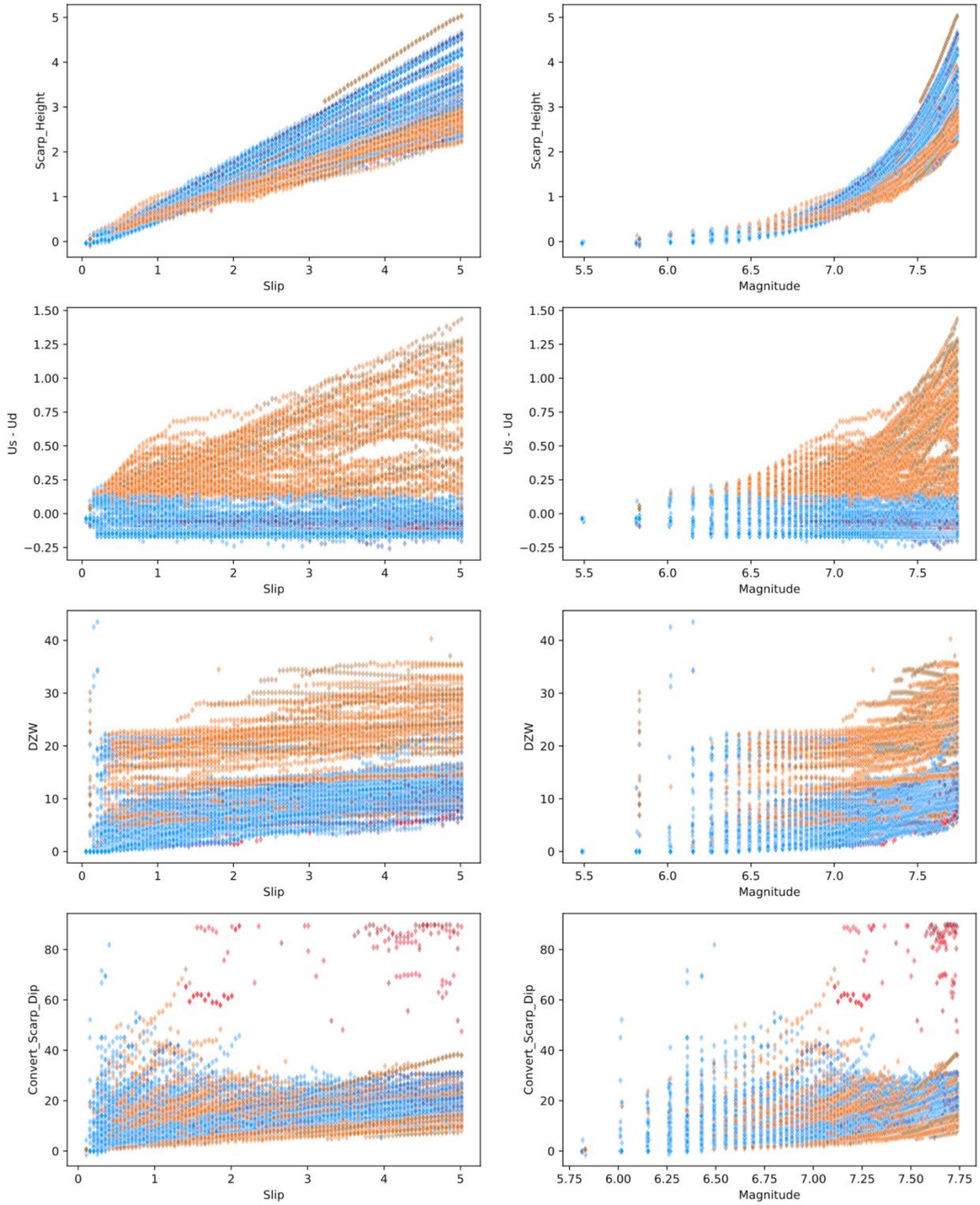

Figure S11: Heterogeneous experiments plotted by the accumulation of slip (*left*) and estimated earthquake magnitude (*right*) by the scarp height, uplift, DZW, and scarp dip (*top to bottom*).

Cohesive Top Unit: 189 experiments

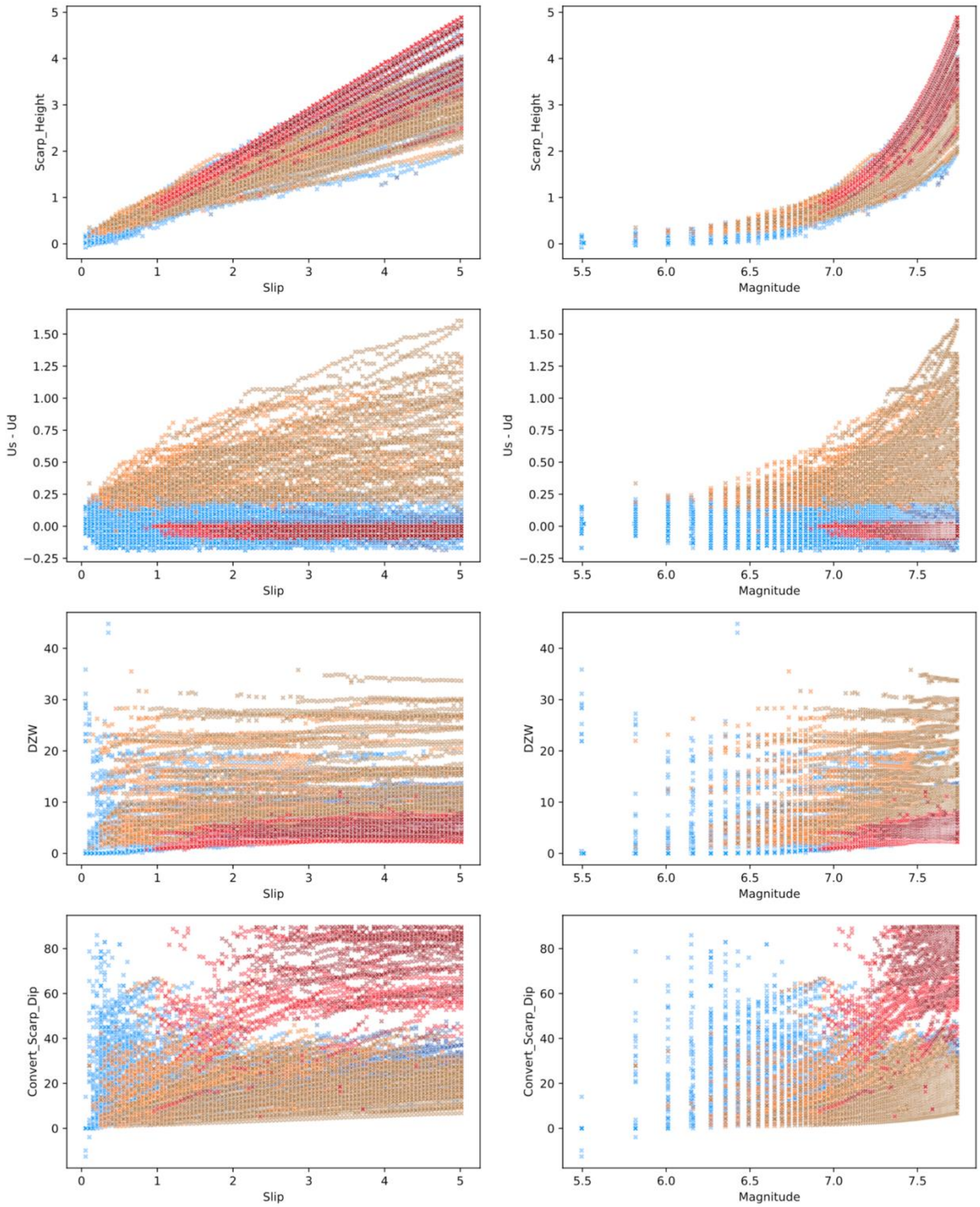

Figure S12: Heterogeneous experiments plotted by the accumulation of slip (*left*) and estimated earthquake magnitude (*right*) by the scarp height, uplift, DZW, and scarp dip (*top to bottom*).

Alternating Strong/Weak Sediment Layers: 9 experiments

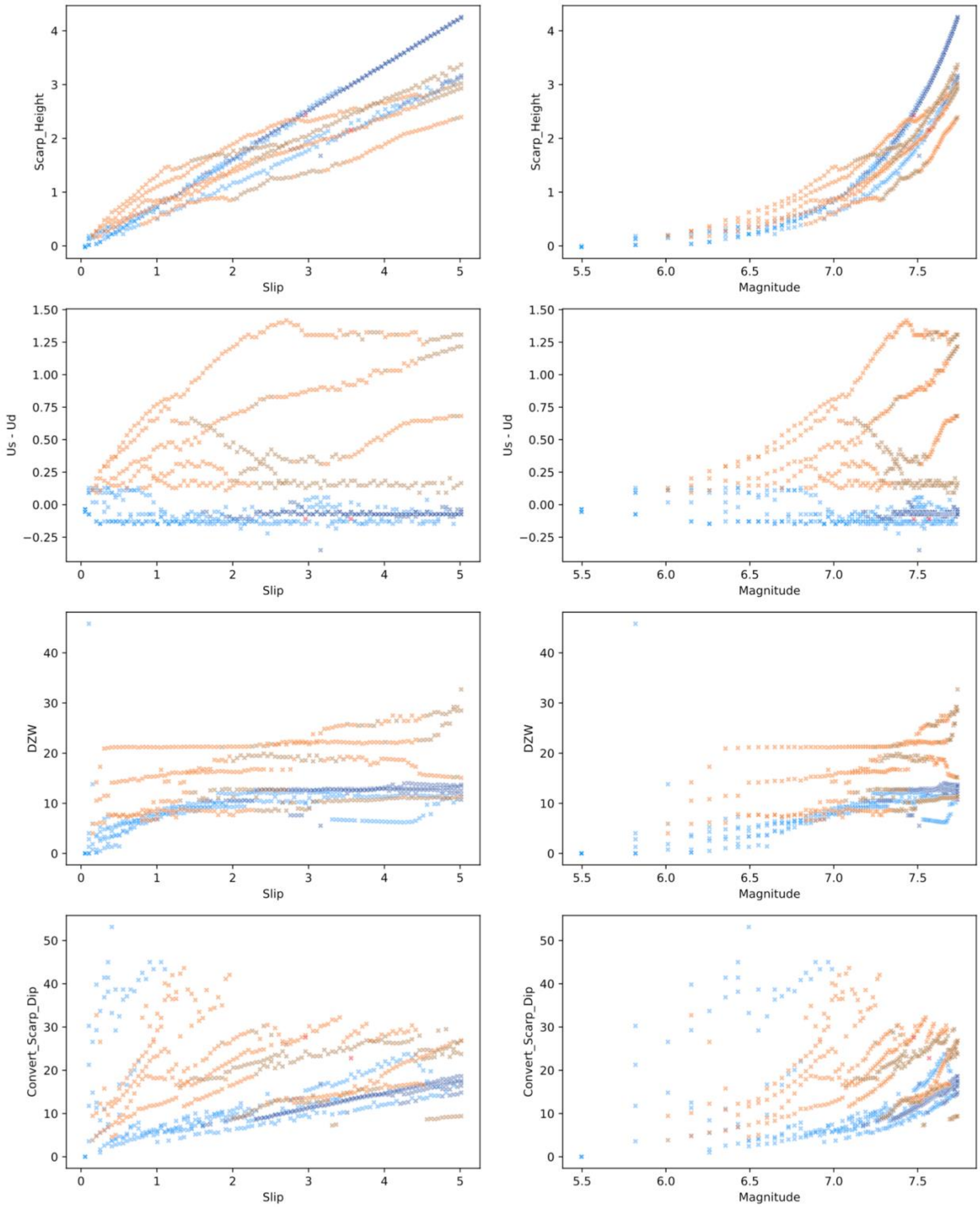

Figure S13: Heterogeneous experiments plotted by the accumulation of slip (*left*) and estimated earthquake magnitude (*right*) by the scarp height, uplift, DZW, and scarp dip (*top to bottom*).

Correlation coefficient plots for: Slip, Scarp Height, $U_s - U_d$, DZW, and Scarp Dip.

Scarp Class:

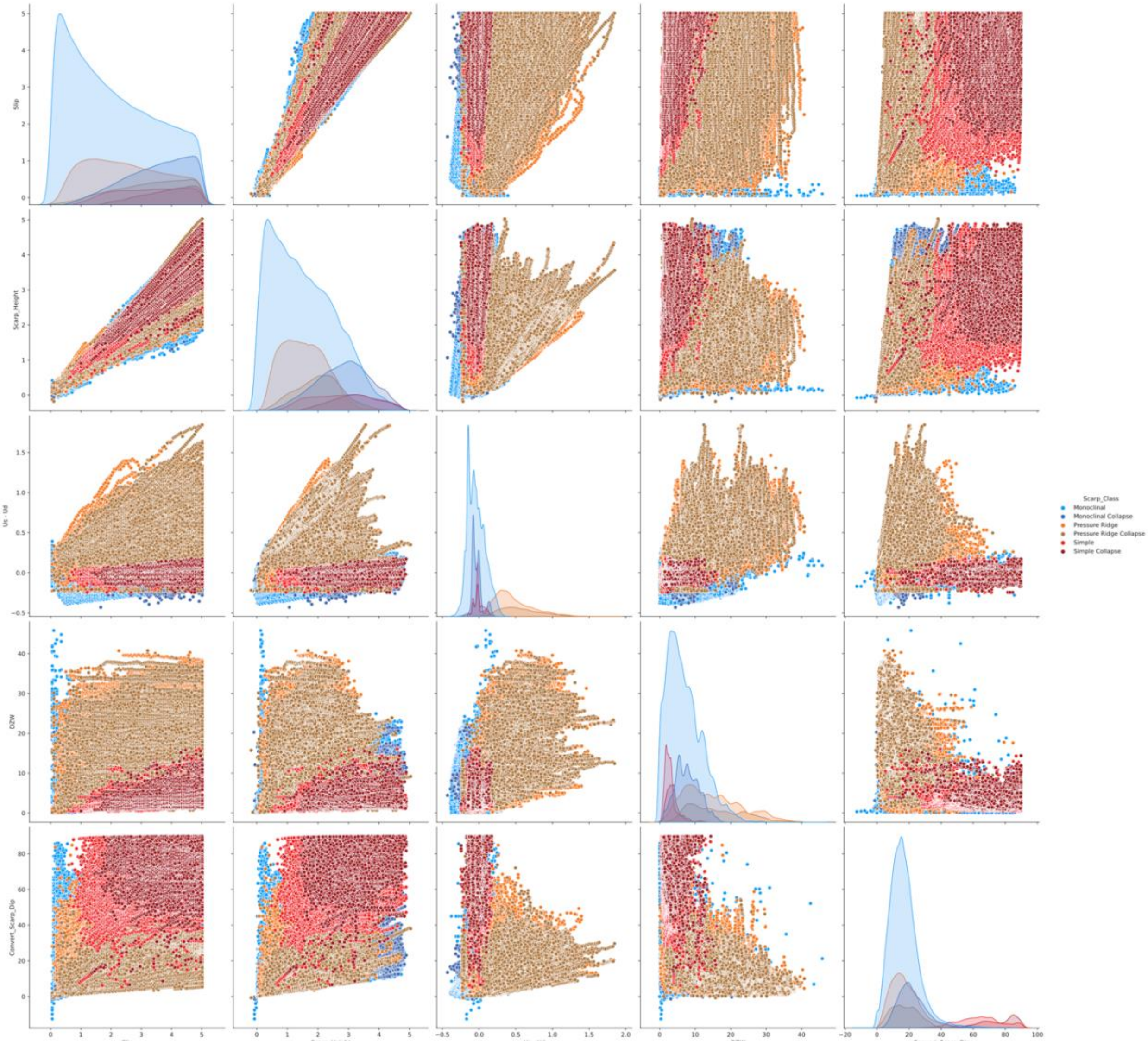

Figure S14. Correlation coefficient plots of the amount of slip, scarp height, $U_s - U_d$, DZW, and scarp dip colored by scarp class.

Sediment Depth:

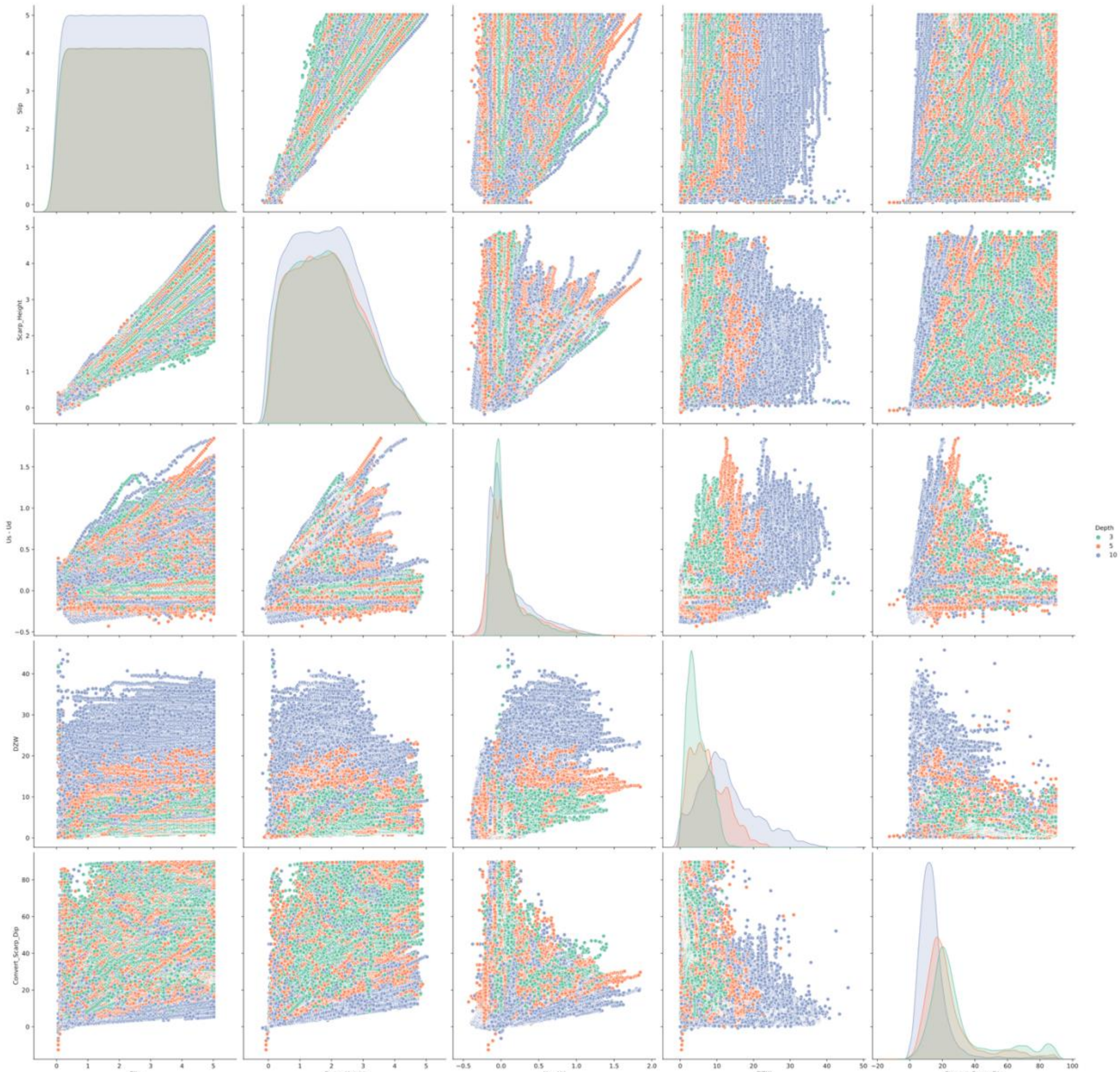

Figure S15. Correlation coefficient plots of the amount of slip, scarp height, $U_s - U_d$, DZW, and scarp dip colored by sediment depth.

Sediment Density:

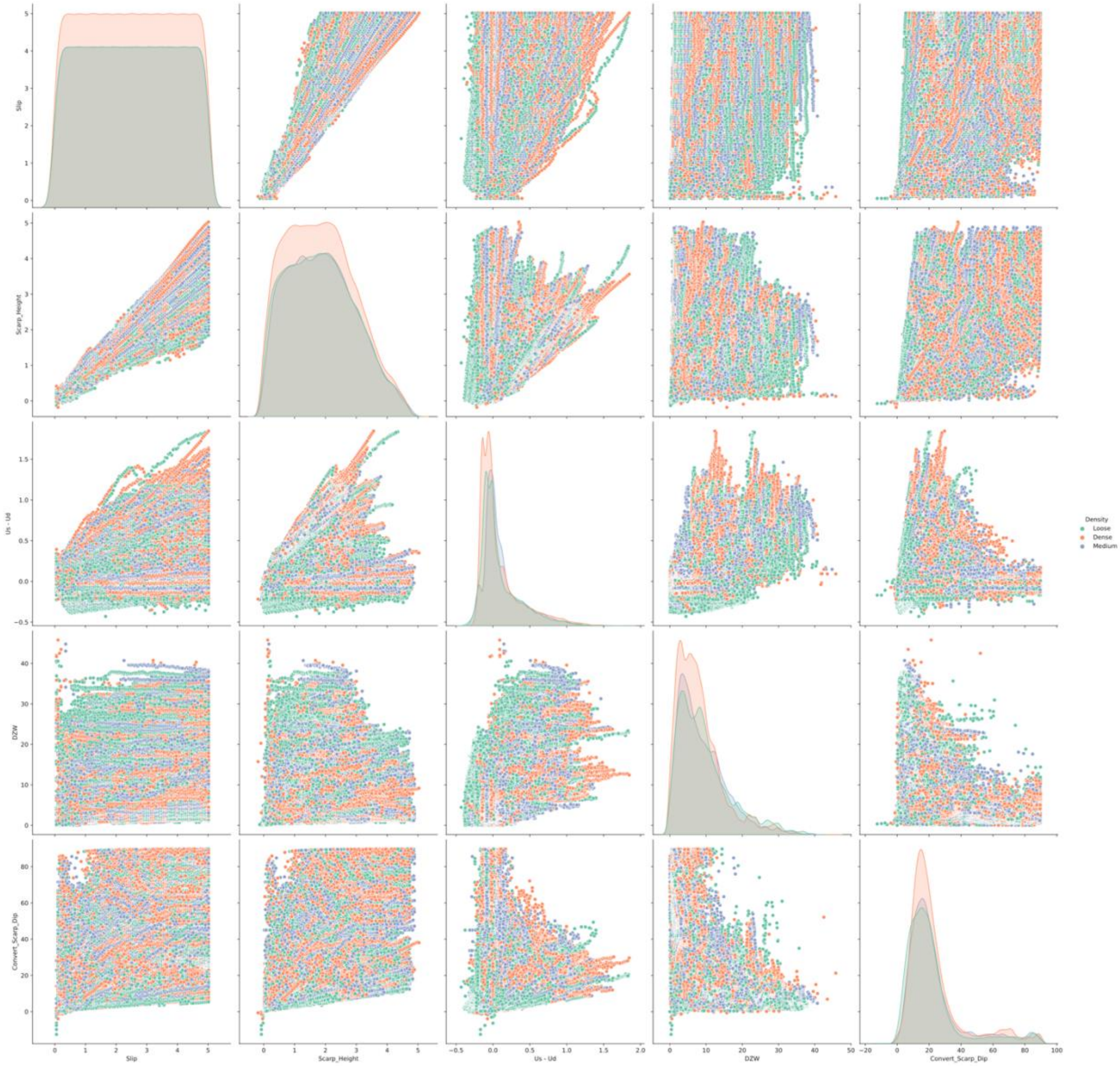

Figure S16. Correlation coefficient plots of the amount of slip, scarp height, $U_s - U_d$, DZW, and scarp dip colored by sediment density.

Sediment Strength:

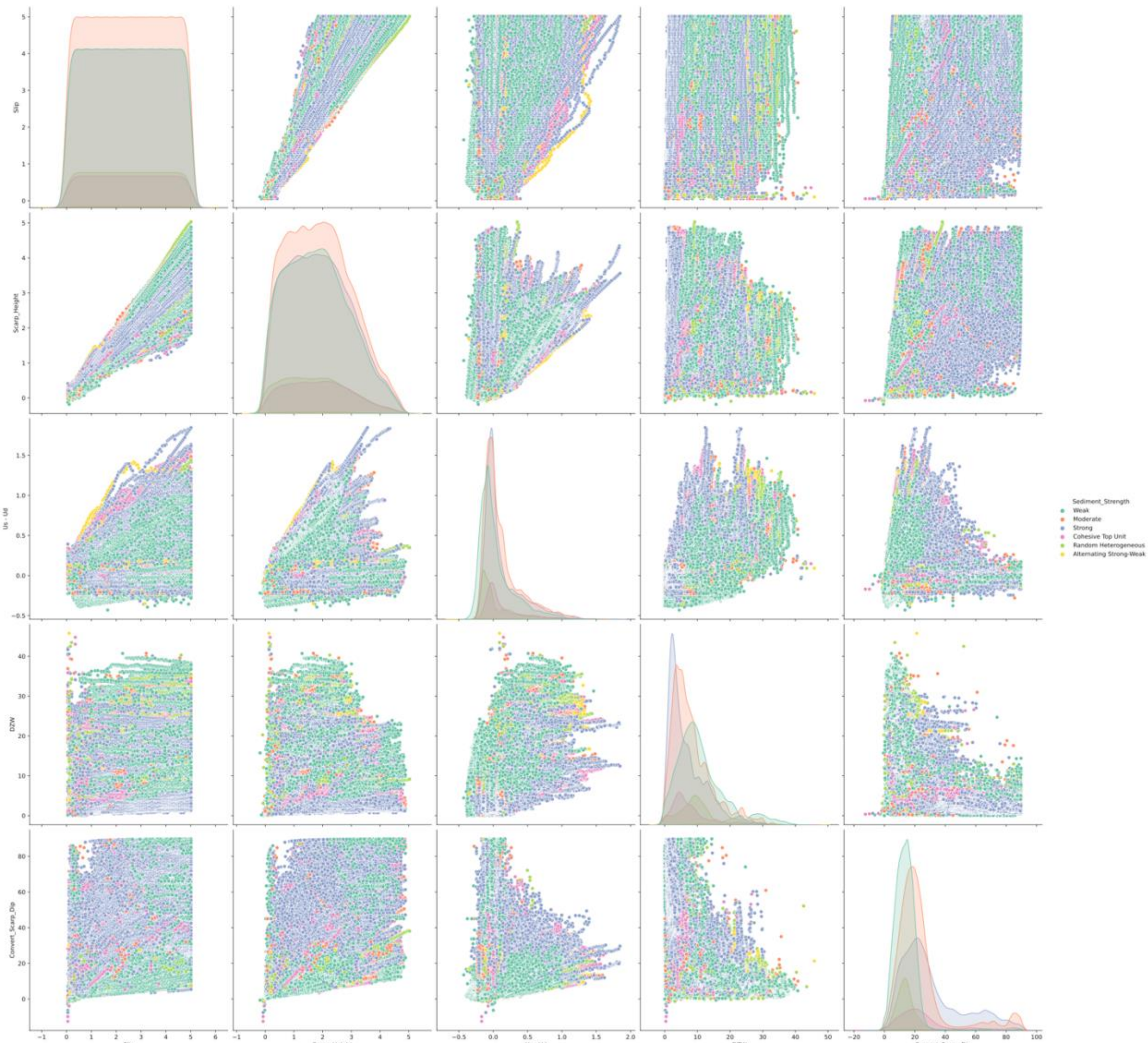

Figure S17. Correlation coefficient plots of the amount of slip, scarp height, $U_s - U_d$, DZW, and scarp dip colored by sediment strength.

Fault Dip:

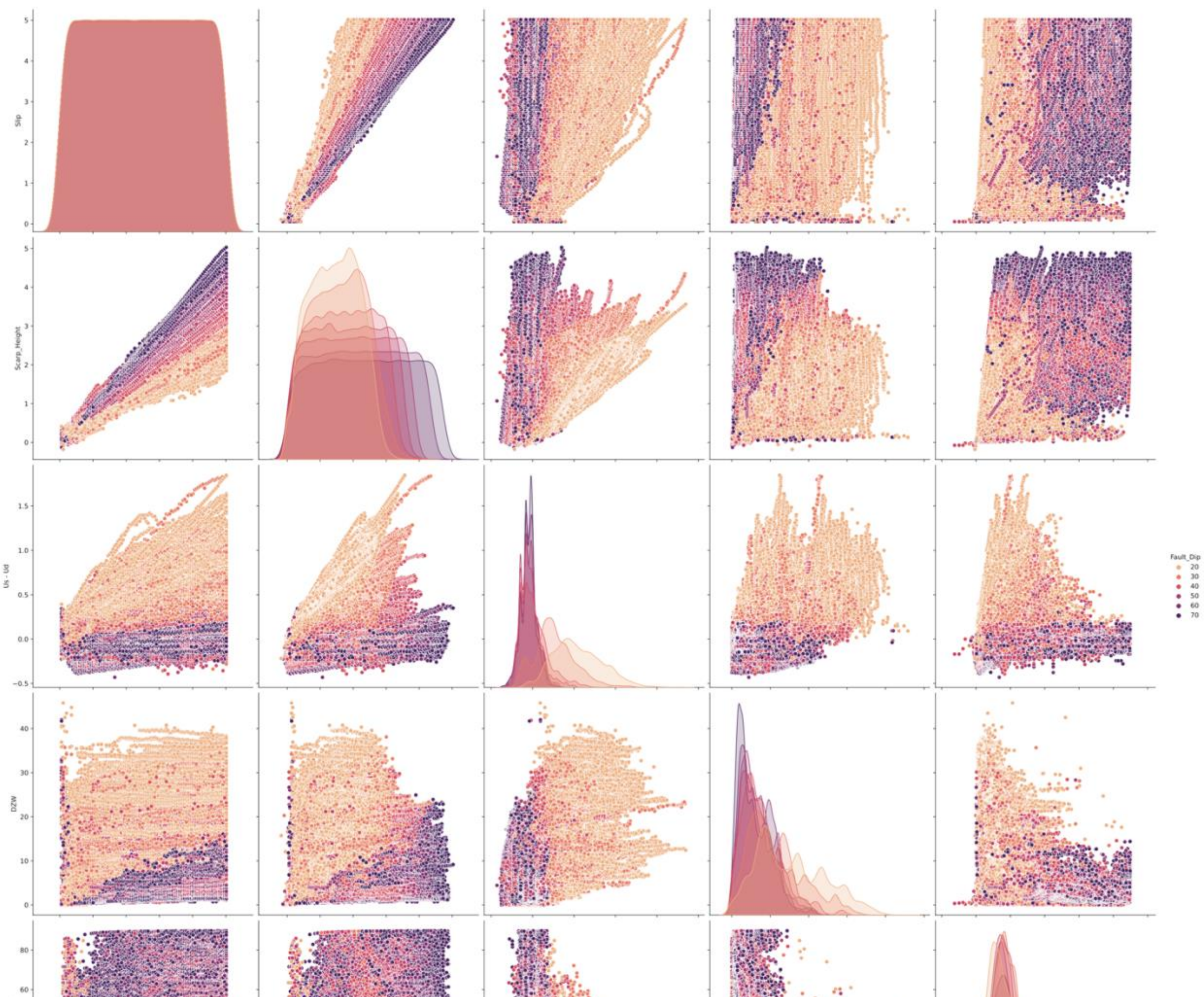

Figure S18. Correlation coefficient plots of the amount of slip, scarp height, $U_s - U_d$, DZW, and scarp dip colored by fault dip.